Chemosphere 307 (2022) 135721

Contents lists available at ScienceDirect

Chemosphere

journal homepage: www.elsevier.com/locate/chemosphere

Delineation of highland saline groundwater sources in Ba'kelalan region of NE Borneo to improve the salt-making production using geochemical and geophysical approaches

Stephan Ongetta [a,b], Prasanna Mohan Viswanathan [a,b,*], Chidambaram Sabarathinam [c], Nagarajan Ramasamy [a,b], Clem Kuek [b,d]

[a] Department of Applied Sciences, Faculty of Engineering and Science, Curtin University Malaysia, CDT 250, 98009, Miri, Sarawak, Malaysia
[b] Curtin Malaysia Research Institute (CMRI), Curtin University Malaysia, CDT 250, 98009, Miri, Sarawak, Malaysia
[c] Water Research Center, Kuwait Institute for Scientific Research, Kuwait
[d] School of Earth and Planetary Sciences, Curtin University, Bentley, Western Australia, Australia

HIGHLIGHTS

- First integrated approach to address salinity issue in groundwater of the Ba'kelalan region.
- Seasonal changes in groundwater recharge affects the salinity in the existing wells.
- Dissolution of evaporites is the key process for the salinization of groundwater.
- Subsurface fault system facilitates the movement of brine groundwater.
- Identified perched aquifer is a promising location for future wells in salt-making.

GRAPHICAL ABSTRACT

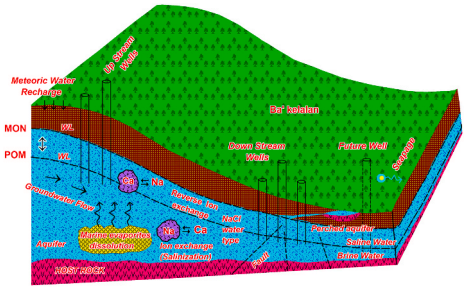

ARTICLE INFO

Handling Editor: Derek Muir

Keywords:
Salinization
Evaporites
Ion exchange
Isotope
Resistivity
Borneo

ABSTRACT

The extraction of mountain salt from the saline waters is the basic livelihood of the Ba'kelalan communities of Sarawak. The current integrated approach is the first attempt to study the sources and geochemical processes of the saline groundwaters in this mountain region. Hence, in this study, saline groundwater samples from five existing wells in different seasons were analysed for hydrochemical parameters and multi-isotope composition ($\delta^{18}O$, δD, $\delta^{34}S$, $\delta^{11}B$ and $\delta^{37}Cl$). The significant increase in TDS, EC and salinity was due to seasonal variation and fluctuation in water level based on hourly, daily and monthly observations. The geochemical ratios and the statistical techniques revealed that the salinity was due to the dissolution of marine evaporites as a dominant process, coupled with other factors such as water-rock interaction, ion exchange and sulphate reduction. From the isotopic signatures, it was inferred that the origin of saline groundwater was from the intense dissolution of marine evaporites such as halite dissolution and oxidation of -sulphide (pyrite). 2D electrical resistivity and seismic refraction methods were used to identify the lithological variations, depth of potential sources of saline groundwater, and the subsurface structures. It was inferred the probability of a conductive zone at a depth of 1–14 m, from which the saline groundwater plume migrates towards the perched aquifer. The presence of

* Corresponding author. Department of Applied Sciences, Faculty of Engineering and Science, Curtin University Malaysia, CDT 250, 98009, Miri, Sarawak, Malaysia.
E-mail address: prasanna@curtin.edu.my (P. Mohan Viswanathan).

https://doi.org/10.1016/j.chemosphere.2022.135721
Received 12 February 2022; Received in revised form 30 June 2022; Accepted 11 July 2022
Available online 16 July 2022

subsurface faults facilitated the movement of hypersaline groundwater from the saturated zone to the surface. The outcome of the study will support the dependent community to enhance their commercial salt production.

1. Introduction

Salinization is a worldwide environmental phenomenon that has significantly impacted our lives through the alternation of chemical compositions in groundwater resources, degradation and increased cost of water supply for domestic purposes (Walter et al., 2017; Kura et al., 2018; Vishwakarma et al., 2018; Thivya et al., 2021), soil salinization (Li et al., 2018), agriculture (Mejri et al., 2018; Pholkern et al., 2018; Chidambaram et al., 2022a), infrastructures and industries (Mateo-Sagasta et al., 2017; Li et al., 2019a; Zhang et al., 2020), and it has caused severe health problems (Vengosh, 2014; Quattrini et al., 2016; Mgbenu and Egbueri, 2019; Mahalakshmi et al., 2022). Nonetheless, saline groundwater possesses a vital role in various processes such as subsurface dolomitization and de-dolomization processes (Ercan et al., 2019; Karakaya et al., 2019), the formation of sediment-hosted ore deposits (Busico et al., 2018), and hydrocarbon migration (Boschetti et al., 2011; Dezayes et al., 2015; Özdemir, 2018).

The natural occurrence of saline groundwater resources in highlands are beneficial in many ways such as maintaining ecosystem and habitats of aerobic microorganism, thermo-mineralized groundwater that are curatives for various diseases, besides serving as tourist attractions, industrial application and mountain salt production (WWF, 2005; Van Weert et al., 2009; Vishwakarma et al., 2018). In highland tropical zones, aquifers tend to have a longer residence time of effective recharge considering the higher precipitation rates (Aghazadeh et al., 2017; Mattos et al., 2018a; Wirmvem et al., 2020). Bawoke et al. (2019) found that the water type evolved from Ca–Mg–HCO_3 to Na–HCO_3 with a substantial increase in salinity from the recharge zone at the highland plateau to the discharge zone adjoining the rift valley. The physical parameters, major ions and nutrients of the groundwater and springs from the Himalayan region illustrated that geogenic factors govern the major geochemical processes. The geochemical processes include ion exchange processes, dolomite and calcite dissolution and the identified process was also supported by water type dominated by Ca–HCO_3 and HCO_3 (Vishwakarma et al., 2018).

Groundwater hydrochemistry provides researchers with all the vital information to understand the different hydrochemical processes over space and time such as water-rock interaction (Prasanna et al., 2017; Esmaeili et al., 2018; Awaleh et al., 2020; Wu et al., 2020), cation exchange (Zaidi et al., 2015; Pisciotta et al., 2019; Sivakarun et al., 2020), evaporation (Liu et al., 2016; Barzegar et al., 2018; Mattos et al., 2018b), oxidation (Mirzavand et al., 2020a) and anthropogenic activities (Liu et al., 2019; Bawoke et al., 2019; Adithya et al., 2020; He et al., 2022). Subsurface salinity processes leading to brine formation are complex due to various factors that occur either from natural processes or human activity (Sarikhani et al., 2015; Engle et al., 2016; Sun et al., 2016; Alekseeva and Alekseev, 2018; Mattos et al., 2018b; Sefie et al., 2018; Li et al., 2019a; He et al., 2022). Natural processes include the influences of the geochemical processes, hydrological system, the diagenetic formation of hydrous minerals (water-rock interaction, precipitation, and dissolution of evaporite deposits) (Mejri et al., 2018), interstitial seawater (connate waters) trapped during original sediment deposition (Han et al., 2018; Duan et al., 2022), saline water flowing from adjacent or underlying aquifers (Liu et al., 2016; Van Engelen et al., 2018), membrane filtration of shales (Engle et al., 2016) and geothermal activity (Chabaane et al., 2017; Awaleh et al., 2018, 2020; Duan et al., 2022). Several anthropogenic sources include irrigation return flow, road de-icing salts, discharge of brine, industrial and agriculture wastewater (Mateo-Sagasta et al., 2017; Jia et al., 2018; Li et al., 2019b; Chidambaram et al., 2022a).

More than 90% of the dissolved solids in groundwater can be attributed to 8 major ions, for instance, Na^+, Ca^{2+}, Mg^{2+}, K^+, Cl^-, SO_4^{2-}, HCO_3^- and CO_3^{2-} (Urrutia et al., 2021). A high concentration of SO_4^{2-} in groundwater causes its development into an antioxidant agent with higher ionic activity, behaving as an essential role in water-rock interaction. The increased dissolution capacity in the groundwater system promoted by sulphate mobilization and dissolution of pyrite consequently causes calcium and iron enrichment in the water. Groundwater contamination by nutrients (NO_3^-, NO_2^-, NH_4^+, NH_3N and NH_3) are commonly caused by land use activities such as fertilizer application, sewage leakage, redox conditions and decomposition of organic matters in sediments (Ehya and Marbouti, 2016; Esmaeili et al., 2018; Ha et al., 2019; He et al., 2022). A humid environment with well-developed drainage system can selectively remove cations from weathered rocks and soils more rapidly (Hem, 1985).

Stable isotopes are valuable tracers in determining the source and mechanism of salinization of water due to their stability over time (Isawi et al., 2016; Awaleh et al., 2018; Bawoke et al., 2019; Li et al., 2019c; Ammar et al., 2020; Alexeeva et al., 2020; Mirzavand et al., 2020b; Szynkiewicz et al., 2020; Duan et al., 2022; Zhang et al., 2022). Isotopic tracers are commonly used to delineate fluid origins and chemical modifications. For instance, oxygen and hydrogen isotopes are used for tracing the origin of waters, the nature of the recharged fluids and the effect of water-rock interactions (Farid et al., 2015; Gil-Márquez et al., 2017; Banda et al., 2019; Xiang et al., 2019; Ninu Krishnan et al., 2022). Groundwater sample enriched with $\delta^{18}O$ and $\delta^{2}H$ along the evaporative line suggests the possibility of evaporation of the water prior to recharge (Bawoke et al., 2019; Chidambaram et al., 2022b; Duan et al., 2022). The relationship between $\delta^{18}O$, $\delta^{2}H$ and salinity was used to identify salinization pathways, transport and origin of solutes in groundwater (Liu et al., 2016; Han et al., 2018; Mattos et al., 2018a; Xiang et al., 2019). The $\delta D - \delta^{18}O$ relationships had been used for calculating the mixing ratio between freshwater and saline or brine, investigation of seawater evaporation and up coning processes (Thivya et al., 2016; Mirzavand et al., 2020b; Duan et al., 2022; Zhang et al., 2022). Chloride isotopes are commonly used to define salinity sources, mixing of different waters, and water-rock interaction (Du et al., 2016; Thivya et al., 2016; Sherif et al., 2019; Ercan et al., 2019; Awaleh et al., 2020). The tracer element, boron and its isotope $\delta^{11}B$ in saline groundwater can help to identify geological processes and its origins such as dehydration and metamorphism during tectonic events, water-rock interaction, wastewater recharge, relics of evaporated seawater (brines), magmatism and geothermal (Musashi et al., 2015; Martin et al., 2016; Ercan et al., 2019; Han et al., 2018). Additionally, $\delta^{34}S$ is used in determining the origin of sulphate, salinization where usually, sulphate reduction and oxidation leads to enrichment and depletion in $\delta^{34}S$, respectively (Mirzavand et al., 2020a). Wirmvem et al. (2020) found that isotopic composition in highland on a regional scale is controlled by altitude effect, where $\delta^{18}O$ and $\delta^{2}H$ values of precipitation decrease with increasing altitude and rainout effect.

Geophysical methods have been widely used for various hydrogeological exploration as they are relatively inexpensive, non-invasive, and efficient and can be used to find solutions to other problems related to natural environments such as engineering, mining, hydrology, and natural hazard assessment (Araffa et al., 2017; Anomohanran et al., 2017; Nazaruddin et al., 2017; Akinbiyi et al., 2019; Glas et al., 2019; Thapa et al., 2019). The electrical resistivity of a geological formation defines the physical characteristics by understanding the flow of electric current through the subsurface formation. The factors influencing electric flow are site-dependent, such as lithology, porosity, water content, burial compaction, the conductivity of electrolyte within a rock, and groundwater salinity (Rehman et al., 2016; Mohamaden et al.,

2016; Farid et al., 2017; Selvam et al., 2021). Sedimentary rocks are relatively more porous and have good saturated thickness, typically with a low resistivity value from 10 to 1000 Ω m, compared to igneous and metamorphic rocks (>1000 Ω m) (Thapa et al., 2019). The resistivity for freshwater varies from 10 to 100 Ω m, while seawater or brine has a very low resistivity of about 0.2–1 Ω m due to a relatively higher salt content (Chabaane et al., 2017; Gómez et al., 2019). In a hydrological investigation, the water level depth can also be determined by acquiring seismic *P*-waves travel time refracted from the interface between two layers of different velocities (Desper et al., 2015; Azhar et al., 2019; Oskooi et al., 2019). *P*-waves velocities depend on the signal wavelength and saturation stage of the rock fluid system through which the wave travels (Glas et al., 2019). The compilation research of *P*-wave velocity values for fully saturated layers ranged between 1200 m/s and 2250 m/s (Desper et al., 2015; Araffa et al., 2017; Alhassan et al., 2018; Azhar et al., 2019). Thus, the combination of 2D resistivity and seismic refraction methods proves to be the most suitable for a hydrogeological investigation by minimizing the ambiguity (Aizebeokhai et al., 2016; Farid et al., 2017; Mainoo et al., 2019).

Saline groundwater in the Ba'kelalan area (the focus of the current study) has been used since unrecorded time for commercial salt production due to its very high salinity. Based on Haile (1962), various salt springs occur in the mountainous highland from Lao Miatu, Bario (Kessler et al., 2019), and Ba'kelalan, which are drained by the headwaters of the Baram and Trusan rivers. Mountain salts produced in this region have a high market value and serve as the basic income for the community in this region. The Ba'kelalan salt is produced in the remote highlands of northern Sarawak by the isolated communities of Lun Bawang since undocumented history. The saltwater is extracted from nearby wells and poured into a tank above the fire stove fuelled by wood. Salt crystals begin to appear slowly, and these crystals are continually stirred and turned over until the residual salt completely solidifies. The whole process requires an entire five-day period, with an average production of 40 kg of salt a week. When the salt forms pale patches and is white in colour, it is then collected from the bottom of the tank and dried. Subsequently, the salts are preserved in a wrapped bamboo or plastic package. In the village of Buduk Bui in the Ba'kelalan area, salt makers have observed a decline in the water level in the existing wells in recent years. This brings the sustainability of continued salt production by the community at the location. The depletion of existing wells happens especially during the post-monsoon season, where less rainwater recharge occurs. Besides, the limited number of wells in Buduk Bui is not sufficient to meet the commercial salt demand in the lowland, and there is a need for new wells to be discovered. Hence, the current research tries to address the issue and solve the needs of the community despite the availability of wells. This is done by integrating other techniques to have additional information on the subsurface with the following objectives: (1) to evaluate the hydrogeochemical characteristics of saline groundwater during different seasons, (2) to identify the potential sources of saline groundwater using 2D resistivity and seismic refraction methods, (3) to identify the lithological and structural controls on saline groundwater.

2. Study area

The study area, Ba'kelalan (Fig. 1) is situated at an enclosed mountain range in the northeast of Borneo and is located between latitudes 3° 57′ and 4° 04′ N and longitudes 115° 36′ and 115° 38′ E, at an altitude of 910 m above sea level (a.s.l) and 4 km from the borders of Kalimantan, Indonesia. The Ba'kelalan area stretches over approximately 14 km along the upper valley of the Kelalan river and is surrounded by mountainous landscapes as a result of sedimentation, tectonic activities and the subsequent weather of more than 50 million years (Haile, 1962; Hutchison, 2005; Hall, 2013). The mountain ranges are built up mainly by the igneous and metamorphic rock of the Mesozoic to Tertiary age, uplifted and intensely folded sedimentary rocks of the Paleogene age (Hutchison, 2005; Hall, 2013; Van Hattum et al., 2013). These Paleogene Formations are composed of deep-water thinly bedded turbidities of shale, slate, sandstone, calcareous sandstone, and rare limestone and had undergone regional metamorphism (Wang et al., 2016). The highlands are formed by an exceptional thickness of predominantly low-grade regionally metamorphosed, turbiditic sediments of the Rajang Group, which belongs to the Belaga, Mulu, and Kelalan Formations (Hutchison, 2010; Wang et al., 2016; Galin et al., 2017). The annual average rainfall ranges from 2000 mm per year, often exceeding 4000 mm (Kura et al., 2018). The Kelalan river flows through the valley

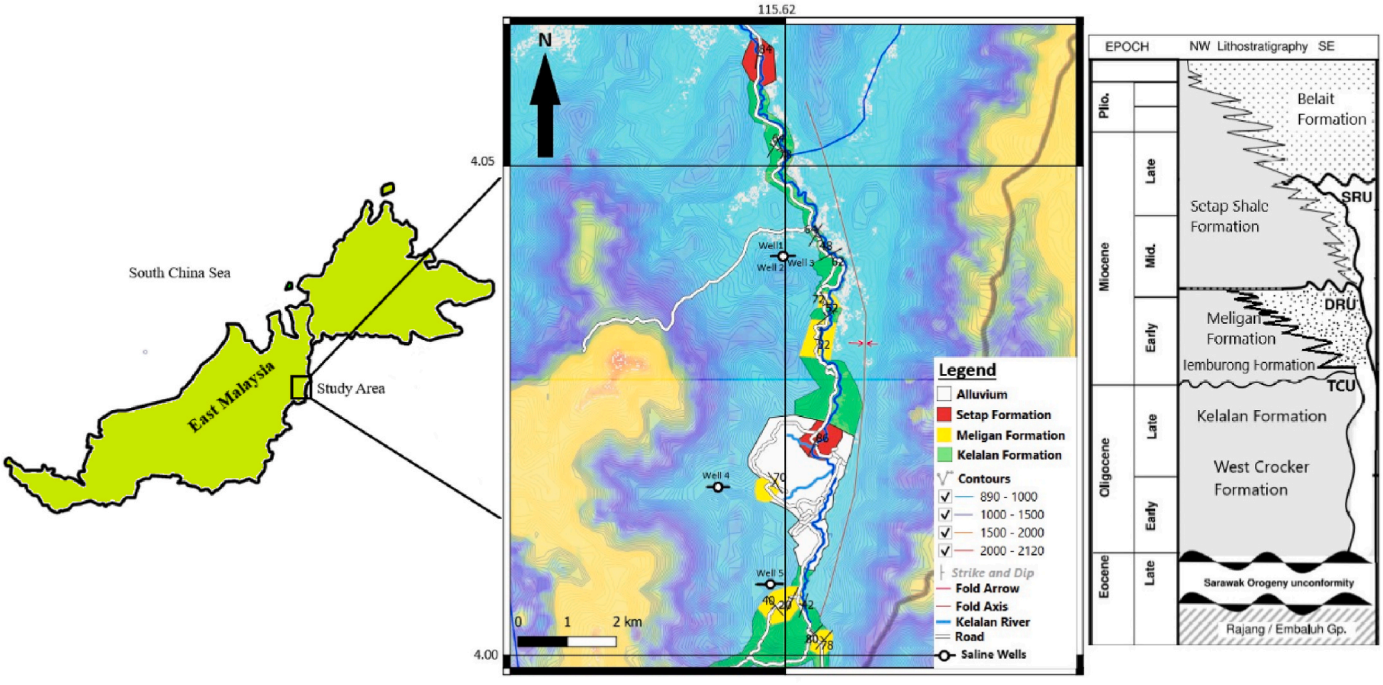

Fig. 1. Geology and saline water well locations with regional stratigraphy of Ba'kelalan (modified from Cullen, 2010).

from south to north direction, is the main drainage channel for the Ba'kelalan area (Fig. 1).

The geology of the study area is composed of the Paleocene basement at the bottom which is made up of metamorphosed turbidites sediments and subsequently overlain by fluvial-deltaic and shallow marine deposits of the Neogene age. It is covered by the recent Quaternary alluvium, composed of sandy and clayey sediments with few gravels formed from river deposits (Haile, 1962; Hutchison, 2005). The Pliocene to Early Miocene aged Setap Shale Formation overlies the Meligan Formation, which is composed of a thick monotonous succession of grey shale and minor turbidities bed of sandstone that is deposited in a shallow marine environment (Wang et al., 2016; Saw et al., 2019). Meanwhile, the Meligan Formation is composed of massive sandstone with minor shale that forms prominent mountain ranges and the suggested age is Oligocene to Late Miocene (Morley et al., 2008; Van Hattum et al., 2013; Abdullah et al., 2017). The sandstone is grey with medium to coarse-grained and in general, quartzose is deposited from the fluviatile-deltaic-shallow environment (Wang et al., 2016). The Kelalan Formation underlies the Meligan Formation and the Setap Shale Formation, forming exceptional escarpments such as Mount Semadoh, Mount Murud, and Mount Batu Lawi (Morley et al., 2008; Wang et al., 2016; Nagarajan et al., 2021). The Kelalan Formation is a folded sandstone of turbiditic siliciclastic with grey slaty shale, siltstone, and rare limestone lenses, and is suggested as Paleocene in age (Wannier, 2009). The sandstone is thinly bedded to massive slightly calcareous, fine to coarse-grained in grey colour. The Kelalan Formation outcrops are found to be exposed in the Ba'kelalan region due to the uplifted and overturned tectonic events (Hutchison, 2010; Nagarajan et al., 2021).

The saline groundwater wells are located at Buduk Bui, Pa'Komap and Punang Kelalan with a total of 5 existing wells. The wells in Fig. 1 are designed using cement and concrete as casing and a PVC pipe to extract the saline groundwater to the surface. The measured groundwater level was approximately 5 m in depth with water level fluctuating between 0.5 and 2 m. The existing wells are located near the foothills and between the valleys with strike of the bedding at NE-SW orientation.

3. Materials and methods

3.1. Sampling and insitu measurements

A total of five dug wells were selected and sampled, in which three wells are located in the downstream with an elevation of 913 m a.s.l (Buduk Bui) and two wells are located in the upstream with an elevation of 948 m and 967 m a.s.l (Pa'komap and Punang Kelalan) respectively. The five existing wells are situated on the foothills and between the valleys with a distance of approximately 6.4 km between the downstream and the upstream. Well 1, 2 and 3 are adjacent to each other at 3 m and 5 m apart, while well 4 and 5's distance is approximately 2.2 km away from each other. The average water level of the existing wells is shallow in depth ranging from 1 to 2.5 m. During sample collection, the water level was measured from the top of the well down to the water surface using a measuring tape. The water samples were obtained by using a bucket to draw the groundwater from the well and were subsequently kept in polyethylene bottles of 100 ml, 500 ml and 5 L, which were rinsed with the water sample beforehand and were stored at a temperature of 4°C until further analysis. The water sample collections were more frequented and detailed, including hourly (<24 h) and on a daily basis. December 2018 and April 2019 samples representing the monsoon (MON) and post-monsoon (POM) seasons were analysed for physical and chemical parameters. The physical parameters such as pH, salinity, temperature, turbidity, total dissolved solids (TDS) and electric conductivity (EC) were measured *insitu* using calibrated analyser probes (Thermo Scientific Orion Star and Turbidity meter). Hourly measurements (<24 h) started from 8 a.m. to 5 p.m. on the 11th December 2018 for well 1, 2, and 3, while daily measurements were taken from 12th until 18th December 2018 for well 1, 2, 3, 4, and 5. In addition, polyethylene bottles were kept for monthly collection from 18th December 2018 to 24th January 2019 and were measured for physical parameters for well 1, 2, 3, and 4. Seasonal sampling of MON was taken in December 2018 and POM in April 2019 for complete chemical analysis for major ions, nutrients, and trace metals.

3.2. Hydrochemical analysis

The collected water samples were filtered with a 0.45 μm filter membrane for further elemental analysis. Major ions such as Cl^- and HCO_3^- were analysed with the titration method (chloride concentration using standard silver nitrate, and bicarbonate using a titration of sulfuric acid) (Ramesh and Anbu, 1996; APHA, 1998). Nutrient analyses (NO_3^-, NO_2^-, SO_4^{2-}, NH_3, NH_3N, NH_4^+, P and PO_4^{3-}) were conducted through the Hach test kit/Spectrophotometer powder pillow method. The major ions (Na^+, Mg^{2+}, Ca^{2+}, K^+) and trace metals (Al, Co, Cu, Cd, Cr, Ba, Pb, Fe, Mn, Sc, Sn, Zn) were analysed using Atomic Absorption Spectrometer (PerkinElmer, AAS). Lithium and boron were analysed using induced coupled plasma – optical emission spectrometry (PerkinElmer, ICP-OES). Prior to analyses, the AAS and ICP-OES were calibrated against the standards and post-calibration for quality control with 95%–99% recovery. Validation of the results was ensured by random cross-checking the values with the standards. Subsequently, the geochemical data were converted into their equivalent or milli equivalence units (meq/L = ppm x valence/molar mass) for interpretation. Next, calculations were made to find the difference between the sum of major cation (Σ cation) and anions (Σ anions), then divided by the sum of all major ions to provide the charge balance error (Clark, 2015). The acceptable error percentage for water analysis is ranged between ±1 and ±10 (Hem, 1985).

$$\text{Charge balance error } (\%) = \frac{\Sigma cation - \Sigma anions}{\Sigma cation + \Sigma anions} x100 \quad (1)$$

3.3. Isotopic analysis

Additional samples of untreated saline groundwater samples were collected in 2L polyethylene bottles for analysis of stable isotopes (^2H, ^{18}O, ^{34}S, ^{11}B, ^{37}Cl). Oxygen and hydrogen (deuterium) isotopes were analysed at the Isotope Hydrology Division of the Center for Water Resource Development and Management (CWRDM), India using continuous-flow isotope ratio mass spectrometry (FINNIGAN DELTA^{PLUS} XP) and converted in per mil delta values (δ‰). Deuterium excess (d) is a function of the $\delta^{18}O$ and δD isotopic composition in water and is calculated as: δD – 8 *$\delta^{18}O$ (Dansgaard, 1964) to determine the relation between evaporation and salinity. The value of stable isotopes is generally represented by δ (expressed in terms of parts per million, ‰) and is defined as (Craig, 1961; Coplen, 1994):

$$\delta(‰) = \left(\frac{R_{sample} - R_{std}}{R_{std}}\right) x\ 10^3 \quad (2)$$

where, R is *D/H* or $^{18}O/^{16}O$ and *SMOW* is the Standard Mean Ocean Water.

^{34}S, ^{11}B and ^{37}Cl were analysed at ActLabs in Ontario, Canada. For ^{34}S, the analysis was carried out using FINNIGAN MAT DELTA^{PLUS} XL IRMS, coupled with Thermo Scientific TC/EA with unit symbol VCDT. Data was corrected and normalized using four international standards: USGS 32, NBS 127, IAEA SO5, IAEA SO6 and calibrated against the standard values of International Atomic Energy Agency (IAEA). The ^{11}B isotope analysis was carried out using a single degassing filament technique on a Thermal Ionization Spectrometry (TIMS). The outcomes were corrected and calibrated against the International Standard NIST SRM 951a and seawater ($\delta^{11}B = 40 \pm 2$). The ^{37}Cl isotope analysis was determined by a continuous-flow ratio mass spectrometry (CF-IRMS) and all the results were corrected and calibrated against the Standard Mean Ocean Bromide (SMOB) as analogue to SMOC for chlorine. The $\delta^{18}O$ and δ^2H stable isotopes were analysed for well 1, 2 and 3 in the

MON season. Whereas, $\delta^{34}S$, $\delta^{11}B$ and $\delta^{37}Cl$ were analysed for only well 1 in the POM season.

3.4. X-ray diffraction method

A representative powdered sample of salt extracted from the saline groundwater was subjected to X-ray diffraction with scan angle (2θ) ranging from 5 to 89°, using a Philip X'Pert X-ray diffractometer. The XRD analysis and interpretation used manual mineral phase identification based on the peak position (*d* spacing, 2θ and relative intensities) with the help of the reference book (Lindholm, 2012). The sample was subjected to an X-ray diffractometer through a range of 2θ from 2° or 3° to40°. The 2θ of each major reflection was measured and compared with analyses of standards.

3.5. Saturation index

Mineral saturation indices have been used to identify mineral dissolution and precipitation processes in groundwater, and to evaluate the degree of equilibrium between water and minerals (Mejri et al., 2018). To calculate the saturation indices, the geochemical program PHREEQC was used to evaluate the hydrochemistry data of the groundwater (Parkhurst and Appelo, 1999; Banda et al., 2019). Saturation indices are computed from the following equation:

$$SI = Log\ (IAP/\ Ks) \quad (3)$$

Where IAP is the ion activity product and Ks is the solubility product constant of the minerals.

3.6. Statistical analysis

Voluminous hydrochemical datasets are reduced and grouped based on similar characteristics using statistical methods. Most researchers have adopted multivariate statistical analyses such as correlation analysis, principal component analysis and hierarchical cluster analysis, which provide a reliable approach to recognise and interpret the complex groundwater chemistry (Thivya et al., 2015; Walter et al., 2017; Kura et al., 2018; Ibrahim et al., 2019; Wu et al., 2020). Principal component analysis (PCA) is a powerful statistical method that has been used to verify the sources of chemical constituents and factors that have influenced the groundwater quality (Singh et al., 2017; Liu et al., 2019). PCA is also used to identify common patterns in hydrochemical data distribution, reduce the initial dimension of data sets and facilitate interpretation (Islami et al., 2018; Pisciotta et al., 2019). In this study, PCA was applied using Statistical Package of Social Studies (SPSS) version 22. The software was used to obtain the correlation matrix and principal components (factors) were extracted with Eigen value of 1. The varimax rotation method was adopted to extract the rotated factors with their percentage of total variance (Adithya et al., 2020). The factor loadings are used to derive the factor score coefficients and thus for each sample, factor scores are computed by multiplying the factor score coefficient by using the standardised data in a matrix. A factor score of >+1 denotes a strong influence on the process. Areas with very negative values (<-1) are almost completely untouched by the process, whereas areas with scores close to zero are moderately influenced (Nepolian et al., 2022).

3.7. Geophysical method

The 2D resistivity profiling was conducted using ABEM Terrameter SAS1000 resistivity system, where the selected types of arrays could be transferred to an internal switching circuit that was controlled automatically and 4 appropriate electrodes were selected for each measurement. The 2D resistivity method was carried out using the Wenner array on a total of five traverse lines which consisted of 42 electrodes aligned collinearly. In each profile, the electrode spacing chosen was 2.5 m with a spread length of 105 m, laid perpendicular to the bed strike of NE-SW direction, and elevation varied from 820 m to 880 m above sea level. A total of 5 profiling was conducted across the study area site, where one profile was conducted on the operating wells, one profile on the old existing wells, and three profiles on the perched aquifer on the lower elevation.

A seismic refraction survey was conducted using ABEM TERRALOC PRO 2 seismograph to map the subsurface features in the study area. The seismic refraction survey was conducted with 5 m geophone spacing and 24 geophones on a straight line. There were 7 shot points located at minus (−) offset, 1st and 2nd geophones, 6th and 7th geophones, 12th and 13th geophones, 18th and 19th geophones, 23rd and 24th geophones and plus (+) offset. The survey lines stretched over between flat ground and sloping hillside of the valley region, composed of alluvium loose soil and sand. Lines were shot in forward and reverse order, with a total length of 120 m interval on each survey profile with a total of five profiles. The raw data recorded by the seismograph was transferred for further processing using the SeisImager software. The first step in seismic refraction processing was to identify and manually pick the first break of seismic arrivals. After the first arrival was picked, the file containing the picked files was loaded into the Plotrefa software and converted to travel-time curves. Furthermore, using the time-term inversion and tomographic inversion methods, a 2D velocity model can be generated.

4. Results

4.1. Hourly, daily and monthly measurements

From the <24 h observation (Fig. 2), the average pH value for well 1, 2, and 3 were measured at 6.6, 7.04, and 7.55 respectively. The TDS average values for well 1 (33,380 mg/L), well 2 (30,550 mg/L), and well 3 (27,440 mg/L) were measured respectively. Meanwhile, the average value of EC for well 1 (52,370 μS/cm), well 2 (48,720 μS/cm), and well 3 (44,115 μS/cm) were measured respectively. According to Freeze and Cherry (1979) and water classification based on the TDS and EC, well 1, 2, and 3 were classified as saline water (10,000 to 100,000 mg/L) to brine water (>45,000 μS/cm). The average temperature values for well 1, 2, and 3 were 27.1, 27.4 and 27.4 C°, respectively. The average values for salinity in well 1, 2, and 3 were found to be 34.5, 31.8, and 28.4‰, respectively. The turbidity average values for well 1, 2, and 3 were 18.7, 18.2, and 9.6 nephelometric turbidity unit (NTU) respectively.

In the daily measurement (Fig. 3), the average pH value for well 1, 2, 3, 4 and 5 were 6.7, 7.4, 7.5, 7.1 and 6.9, respectively. The TDS average values for well 1 (33,000 mg/L), well 2 (30,414 mg/L), well 3 (27,500), well 4 (18,860 mg/L) and well 5 (20,860 mg/L) were measured respectively. Meanwhile, the EC values of the samples ranged from 28,800 to 52,500 μS/cm with a mean value of 42,023 μS/cm. In addition, the salinity values ranged from 17.7 to 34.6‰ with a mean value of 27.1‰. The average temperature values ranged from 21.5 to 25.2 °C. The average water level values for all the wells ranged from 0.8 to 2.5 m and the average turbidity values ranged from 1.5 to 42.8 NTU with a mean value of 8.46 NTU.

From the monthly measurement (Fig. 4), the average pH values for well 1, 2, 3 and 4 were 7.4, 7.5, 7.8 and 8.1, respectively. The average values for temperature in well 1, 2, 3 and 4 were ranged from 22.1 to 25.6 °C. Meanwhile, the average TDS values for well 1 (34,448 mg/L), well 2 (34,264 mg/L), well 3 (30,737 mg/L) and well 4 (21,548 mg/L) were measured respectively. The average EC values for well 1 (68,997 μS/cm), well 2 (68,797 μS/cm), well 3 (61,397 μS/cm) and well 4 (43,240 μS/cm) were measured respectively. The average values for salinity in well 1, 2, 3 and 4 were 47.1, 47.1, 41.1 and 27.8‰, respectively.

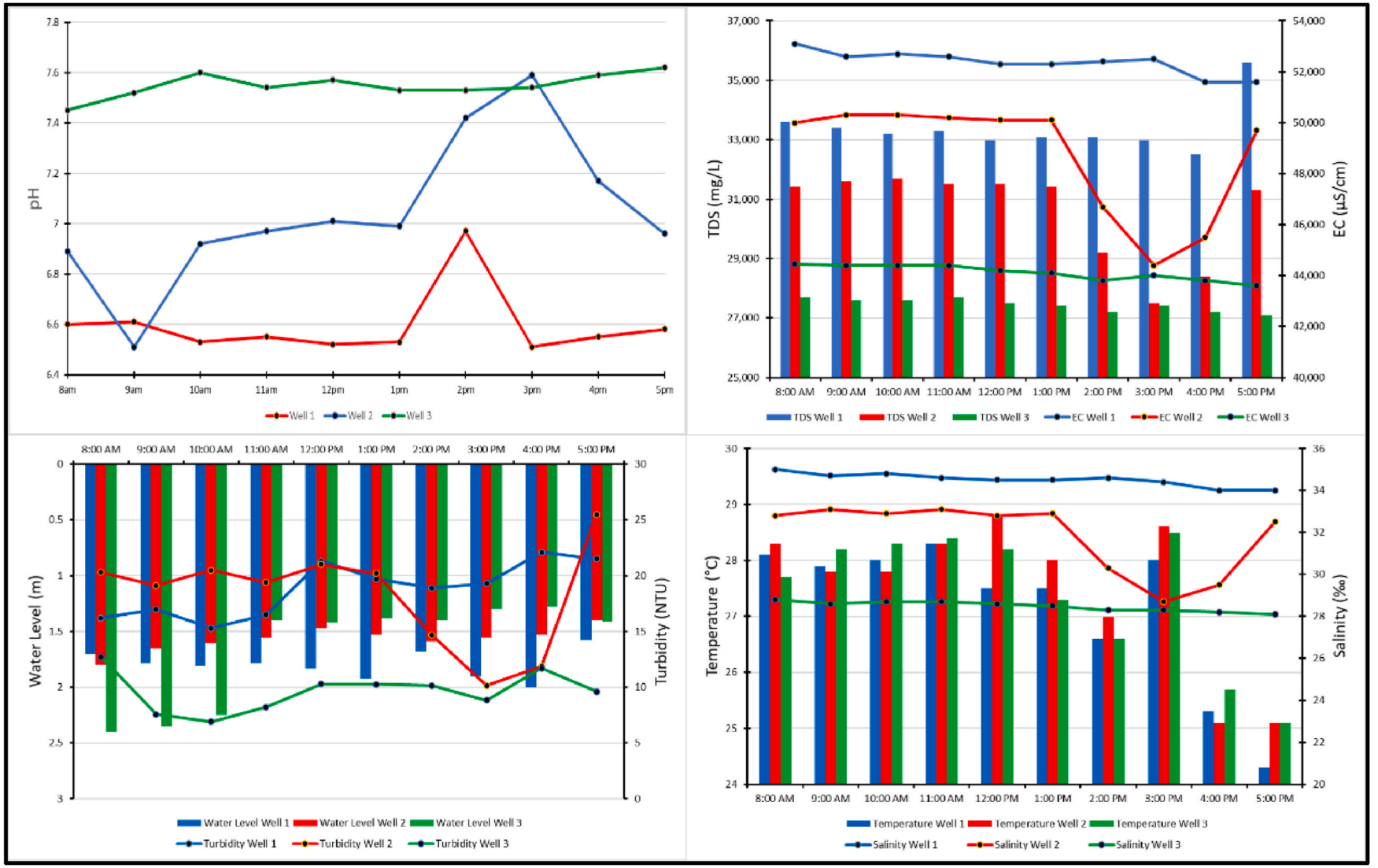

Fig. 2. The hourly measurement for pH, TDS, EC, salinity, temperature, turbidity and water level in the existing wells.

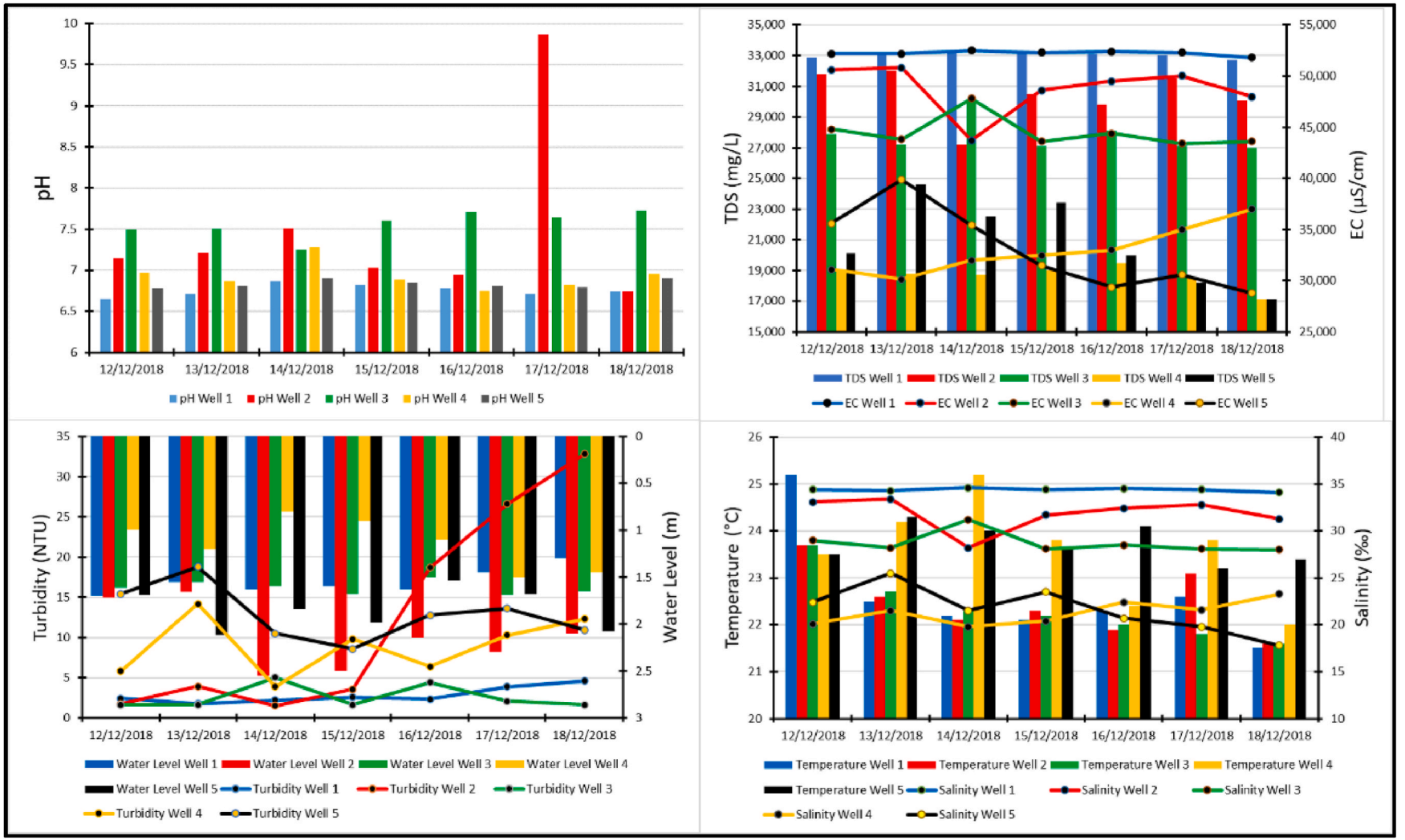

Fig. 3. The daily measurement for pH, TDS, EC, salinity, temperature, turbidity and water level in the existing wells.

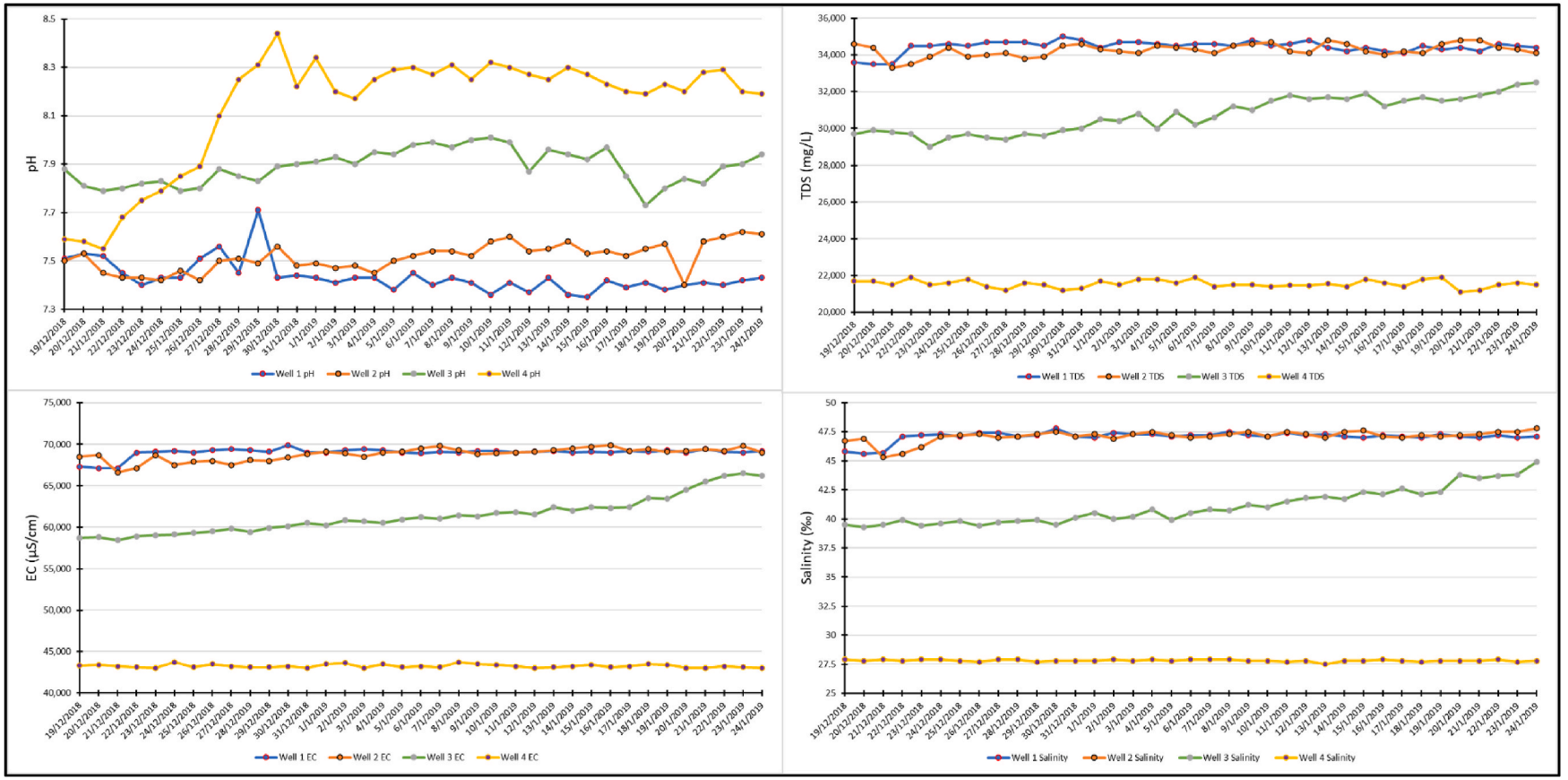

Fig. 4. The monthly measurement for pH, TDS, EC and salinity in the existing wells.

4.2. General geochemistry

The pH values for saline groundwater suggested a slightly acidic to alkaline nature, which varies from 6.7 to 7.7 during MON and 6.5 to 7.3 during POM. Saline groundwater wells in Ba'kelalan have high salinity content with the EC value varying between the seasons with 28,800 to 51,800 μS/cm during MON and 40,500 to 66,500 μS/cm during POM. According to Freeze and Cherry (1979), well 1 and 2 were categorized as brine water, while well 3, 4 and 5 were considered as saline water based on EC values. However, based on TDS values, all groundwater samples were categorized as saline water, with the range of 17,120 to 32,700 mg/L during MON and 10,300 to 33,300 mg/L during POM. It was found that the salinity increased significantly, ranging from 17.7 to 34.1‰ during MON and 25.9–45.2‰ during POM.

For the hydrochemical data in the saline groundwater (well 1, 2, 3, 4 and 5), the concentration of Na^+ ranged from 3,575 to 4,536 mg/L during MON and 6,740 to 14,184 mg/L during POM, respectively. Na^+ was the dominant cation in all the samples for both seasons (Table 1). For all the samples, K^+ concentration ranged between the seasons with 10.4–29.9 mg/L during MON and 24.3–31.8 mg/L during POM, respectively. The Ca^{2+} concentration varies between the seasons with 225.2–430.2 mg/L during MON and 138–245.2 mg/L during POM. Mg^{2+} concentration varies between the seasons with 54.80–138.6 mg/L during MON and 62.8–138.6 mg/L during POM. Cl^- was the dominant anion in all groundwater samples, where its value ranged from 6,534.4 to 8,175 mg/L during MON and 11,547 to 25,450 mg/L during POM. The HCO_3^- concentration varies between seasons with 548–875.5 mg/L during MON, while for the POM, it ranges between 1,085.8 and 1,780.8 mg/L. The order of dominance of major ions in both seasons for the saline groundwater samples is as follows: $Na^+ > Ca^{2+} > Mg^{2+} > K^+ = Cl^- > HCO_3^- > NO_3^- > SO_4^{2-}$.

The SO_4^{2-} concentration ranged from 1 to 2 mg/L during MON and 0.5–1 mg/L during POM. NO_3^- ranged between 0.1 and 19 mg/L during MON and 0.1–1.1 mg/L during POM, respectively. Whereas, the concentration for NO_2^- ranged from 0.1 to 4.3 mg/L during MON and 0.1-0.2 during POM. For NH_4^+, NH_3 and NH_3N, the concentration exhibited similar values, however, ammonia ion (NH_4^+) was the major *N*-species, where it varied from 0.5 to 24.5 mg/L during MON and 4.2–16.7 mg/L during POM. The phosphorous found is normally identified as orthophosphate (PO_4^{3-}), where the water samples exhibited low concentration in both phosphate and phosphorous, with the PO_4^{3-} value varying between 0.3 and 0.7 mg/L during MON and 0.2–0.9 mg/L during POM. Meanwhile, the phosphorous concentration was between 0.1 and 0.2 mg/L during MON and 0.1–0.3 mg/L during POM.

The order for trace metal concentration present in the saline groundwater samples during MON season is as: Sn > Ba > B > Sc > Fe > Cu > Li > Cr > Co > Rb > Zn; meanwhile, for POM season, the order is as: Ba > B > Sc > Sn > Fe > Li > Zn > Co (Table 1). The concentration of Sn in groundwater samples indicates the highest loading during MON, ranging from 16.5 to 22.6 mg/L. However, during POM, the concentration is reduced to 2.2–4.9 mg/L. The groundwater samples for B have values ranging from 2 to 5 mg/L during MON and 1.4–5.3 mg/L during POM. Ba concentration is observed in the range of 8.5–12.8 mg/L during MON and 3.3–7.3 mg/L during POM. The concentration for Sc varies between the seasons as 2.4–3.9 mg/L and 2.3–5.4 mg/L during MON and POM respectively. The Fe concentration varied between 1.3 and 7.2 mg/L during MON and 1–1.2 mg/L during POM.

The XRD of salt sample revealed that halite (Na Cl) is the major component identified by peak positions at 31.61°, 45.35° and 75.16° (93%), along with the minor amount of pyrite (FeS_2) represented at 56.33°(5%) and aragonite ($CaCO_3$) at 27.24°(2%).

The saturation index of the groundwater composition representing the MON and POM seasons indicated that they are undersaturated with the composition of gypsum (−4.27 to −3.35), halite (−4.37 to −2.39) and anhydrite (−4.63 to −3.73). The minerals of barite (−1.35 to 0.39) and magnesite (−0.59 to 0.05) are saturated, while the minerals of aragonite (0.11–0.84), dolomite (0.29–1.88) and calcite (0.14–1.11) are oversaturated.

4.3. Stable isotopes

In Fig. 5, all the data are compared with the Global Meteoric Water Line (GMWL) $\delta D = 8\ \delta^{18}O + 10$, as defined by Craig (1961), and the Local Meteoric Water Line (LMWL) $\delta D = 7.64\ \delta^{18}O + 10$, as defined by Ninu Krishnan et al. (2022). The $\delta^{18}O$ values of the saline groundwater are 6.11‰, 5.06‰, and 3.6‰ for well 1, 2 and 3, respectively, with a mean value of 4.92‰. Meanwhile, the δD values are −17.85‰, −20.32‰ and −24.70‰, with a mean value of −20.95‰. The groundwater samples were depleted with very low d-excess values of −66.73‰, −60.8‰ and −53.5‰ for well 1, 2 and 3, respectively (Fig. 6).

The study area sample has a value of $\delta^{34}S$ at 1‰, which falls on the oxidation sulfide zone (Fig. 7). In Fig. 8, the groundwater sample falls on the dissolution of marine carbonate rocks zone with $\delta^{11}B$ value of 18.2‰. In Fig. 9, the study area sample falls on the dissolution of the marine evaporites zone and is witnessed by the $\delta^{11}B$ versus Cl. In Fig. 10, the saline groundwater sample falls above the evaporation line and has a $\delta^{37}Cl$ value of 0.82‰.

4.4. 2D resistivity survey

Profile R1 was located adjacent to the potential target of the perched aquifer and was marked near the midpoint with a spreading length of 105 m at the NW to SE orientation (Supplementary Fig. 1). The inverse model shows the resistivity value ranging from 120 to 230 Ω m at a depth of <1–4 m towards the NW part. The moderate resistivity ranges between 45 and 70 Ω at a depth of 5–15 m, separating the two groundwater plumes (Supplementary Fig. 2). The lowest resistivity value dominating the nearby perched aquifer (spring) with a value of 2.8 to < 10 Ω m at a depth of 1–14 m.

The traverse profile R2 located adjacent to profile R1 is served to conduct a grid pattern for the target perched aquifer (spring). The topsoil showed the highest resistivity value, ranging from 167 to 505 Ω m at a depth from near-surface to 5 m, mostly on the NW part (Supplementary Fig. 3). The yellow and green colours show the resistivity value of ≈50 Ω m, at the depth of 10–15 m. Towards the SE of the survey line, the lowest resistivity value was from 0.2 to 5.50 Ω m at the depth of 3–13.

Profile R3's resistivity inverse model shows the highest value of 110–300 Ω m, suggesting topsoil at a depth of 0.5–5 m, dominating most of the near-surface across profile R3. The resistivity value of ≈50 Ω m could indicate the sandy layer between the two separated groundwater plumes (Supplementary Fig. 4). Nonetheless, the inverse resistivity model shows the lowest value of 0.3 to <5 Ω m at a depth of 1–8 m, with approximately 5 m width.

Profile R4 shows that the highest resistivity recorded near the surface with a value ranging from 125 to 233 Ω m, covering most of the survey line from depth <1–3.5 m (Supplementary Fig. 5). The marked old well at a distance of 5 m from the mid-point shows very low resistivity value from 2.8 to <10 Ω m, implying that the previous saline groundwater was at a depth from <1 to 15 m.

Profile R5's resistivity inverse model value shows that the highest value of 213–480 Ω m at a depth of <1–3.5 m located near the NW part of the study area (Supplementary Fig. 6). The three existing wells were marked at a distance location near the mid-point of 8 m, 12 m and 14 m. The inverse resistivity model value shows the lowest reading from 2.84 to <6 Ω m at a depth from <1 to 15 m.

4.5. Seismic refraction

Profile S1's primary wave velocity of the topmost layer (violet colour) with the lowest seismic velocities ranges from 727 to 915 m/s (Supplementary Fig. 2). The thickness of the first layer ranges between

Table 1
Chemical composition of saline groundwater in existing wells of Ba'kelalan during monsoon and post monsoon periods (all values of major ions, nutrients and metals in mg/L).

MON	pH	Temp (°C)	TDS (mg/L)	EC (μs/cm)	Salinity (‰)	Turbidity (NTU)	SO_4^{2-}	PO_4^{-3}	P	NO_3^-	NO_2^-	NH_4^+	NH_3	NH_3N	Na^+	K^+	Ca^{2+}	Mg^{2+}	Cl^-	HCO_3^-	Mn	Fe	Ba	Zn	Sc	Co	Cd	Cu	Cr	Rb	Sn	B	Li
Well 1	6.7	21.5	32,700	51,800	34.1	4.5	1	0.7	0.2	0.6	0.1	3.7	3.5	3.1	4512	18.6	378.6	126.6	8175	875.5	BDL	2.8	8.5	BDL	3.9	0.1	BDL	0.4	0.1	BDL	16.5	4.1	0.2
Well 2	6.7	21.6	30,100	48,000	31.3	42.8	2	0.5	0.1	0.7	0.1	24.5	23	19	4536	24.9	430.2	138.6	8075.5	762.5	BDL	7.2	9.7	BDL	2.4	0.1	BDL	0.6	0.1	BDL	18.1	3.6	0.2
Well 3	7.7	21.6	27,000	43,600	28	1.63	1	0.3	0.1	19.1	4.3	0.5	0.5	0.4	4308	10.4	225.2	54.8	7857	603.9	BDL	1.3	11.2	0.2	2.6	0.1	BDL	0.4	0.2	BDL	19.8	5	0.3
Well 4	6.9	22.0	18,770	31,100	19.2	12.3	1	0.4	0.1	0.1	BDL	12.5	11.7	9.7	3875	29.9	285.4	74.6	6875.5	548	BDL	1.7	11.7	0.1	2.4	0.1	BDL	1.6	1	BDL	21.5	2	0.1
Well 5	6.9	23.4	17,120	28,800	17.7	10.9	1	0.4	0.1	0.1	BDL	12	11.2	9.2	3575	25.6	251.2	100.4	6534.4	578.9	BDL	2.1	12.8	BDL	3.9	0.1	BDL	0.6	0.4	BDL	22.6	2	0.1
POM	pH	Temp (°C)	TDS (mg/L)	EC (μs/cm)	Salinity (‰)	Turbidity (NTU)	SO_4^{2-}	PO_4^{-3}	P	NO_3^-	NO_2^-	NH_4^+	NH_3	NH_3N	Na^+	K^+	Ca^{2+}	Mg^{2+}	Cl^-	HCO_3^-	Mn	Fe	Ba	Zn	Sc	Co	Cd	Cu	Cr	Rb	Sn	B	Li
Well 1	6.5	25	33,300	66,500	45.2	14.5	0.5	0.7	0.2	0.2	BDL	16.7	15.7	13	14,184	28.6	240	138.6	25,450	1780.8	BDL	1.1	3.3	0.1	3.7	0.1	BDL	BDL	BDL	BDL	2.2	5.2	0.3
Well 2	6.7	24.9	28,100	56,300	37.4	12.8	1	0.8	0.2	0.3	0.1	14.7	14	11.5	12,064	31.8	245.2	120	21,584	1500.6	BDL	1.1	5.9	0.2	5.4	0.1	BDL	BDL	BDL	BDL	2.4	5.3	0.3
Well 3	6.8	24	25,100	58,900	33.1	8.7	0.5	0.4	0.2	0.1	BDL	4.2	4	3.7	9476	24.9	204.4	106.8	17,859	1256.6	BDL	1	5.5	0.2	2.3	0.1	BDL	BDL	BDL	BDL	3.3	3.6	0.2
Well 4	7.1	23.2	20,800	41,170	26.7	29.7	0.5	0.9	0.3	1.1	0.2	9	8.5	7	7736	26.4	138	82.8	13,458	1195.6	BDL	1.1	6.1	0.3	2.9	0.1	BDL	BDL	BDL	BDL	3.8	1.4	0.1
Well 5	7.3	23.9	10,300	40,500	25.6	2.1	0.5	0.2	0.1	0.2	BDL	4.7	5.7	5.7	6740	24.3	148.2	62.8	11,547	1085.8	BDL	1.2	7.3	0.1	3.2	0.1	BDL	BDL	BDL	BDL	4.9	2.5	0.2

*BDL – below detection limit.

1.5 and 5 m. The second layer is made up of seismic velocity ranges from 1,020 to 1,900 m/s. The thickness of the second layer is ranges between 2.5 and 10 m. The third layer has a velocity ranging between 2050 and 2485 m/s at a depth of <10 m.

Profile S2's first layer shows a velocity ranging from 997 to 1,150 m/s and the thickness of the first layer is ranged from 1 to 8 m (Supplementary Fig. 3). Whereas, the second layer shows the velocity in the range of 1,392 to 2,579 m/s, and estimated to be at a depth of 5–10 m below the surface. The third layer has a velocity ranging from 2,973 to 3,370 m/s at depth of <12 m.

Profile S3's survey line spreading almost perpendicular across profile S1 and profile S2 was used to conduct 3D concept view for the main target perched aquifer which was marked at the distance of 20 m towards NW. The first layer shows a velocity value ranging from 1,002 to 1,150 m/s, with a thickness of 4–6 m. The second layer showing a velocity value of 1,345 to 2,375 m/s with thickness ranging between 1.5 and 10 m (Supplementary Fig. 4). The third layer has a velocity ranging from 2,718 to 3,060 m/s at a depth of 10–25 m.

Profile S4 located next to profile S3 with survey line extending towards SW was used to locate any possibility of extension of the perched aquifer. The first layer shows the velocity value of 209–315 m/s with a thickness ranging between 4 and 10 m, with the center of the profile being thicker (Supplementary Fig. 7). The second layer shows a velocity of 528–846 m/s at a depth of 10–20 m.

Profile S5 was located across all 3 existing wells in the study area. The first layer of the seismic velocity ranging from 524 m/s to 850 m/s and the thickness ranging between 2 and 10 m (Supplementary Fig. 6). The second layer velocity ranges from 1,097 to 2,091 m/s and the thickness ranging between 5 and 9 m. For this location, the water level is estimated to be at a depth of <10 m below the surface. The third layer has a velocity of 2588 m/s at a depth of 15–20 m.

5. Discussion

5.1. Variation in physico-chemical measurements

Well 1, 2 and 3 are located adjacent to each other in the study area and it is found that well 1 has the highest value for most of the physical parameters (TDS, EC and salinity) compared with the rest of the wells. Additionally, from the hourly measurement, all three wells at 10 a.m. (2.2 m) to 11 a.m. (1.4 m) illustrate significant changes in water level that possibly indicate the groundwater recharge.

From the hourly and daily measurements, the acidic nature (pH 6.6) in well 1 caused more dissolution during rock-water interaction which has increased the ionic concentration in the groundwater. Meanwhile, the change in TDS and EC values indicate that both parameters were strongly correlated and relatable to the recharge in the study area (Rusydi, 2018). From the daily measurements, all five wells appeared to have a slight fluctuation value of pH especially for well 2 on 17th December 2018, where a significant increase in pH was observed, with the highest value at 9.8 (Fig. 3). The TDS and EC values were found in well 1 as the most constant and have the highest value compared to the rest of the wells. It was noticed that TDS, EC, and salinity were strongly correlated and decreasing values in TDS and EC for well 2 were observed on 14th December 2018, which corresponded to the decrease in salinity. For the salinity value, well 1 possessed the highest reading while well 4 and 5 recorded the lowest. For turbidity values, well 2 possessed the highest value followed by well 5 > well 4 > well 3 > well 1. Similarly, well 2 dominated the peak value for the water level. Meanwhile, the temperatures for all the wells were constant with values ranging from 21.5 to 25.2 °C.

From the monthly measurements, all three wells emerged to have significant increase values in most of the parameters (Fig. 4). The pH value for well 4 was found to have significantly increased from 20th December 2018 to 30th December 2018, from 7.6 to 8.4 and marked as the highest pH value, followed by well 3 > well 2 > well 1. Furthermore,

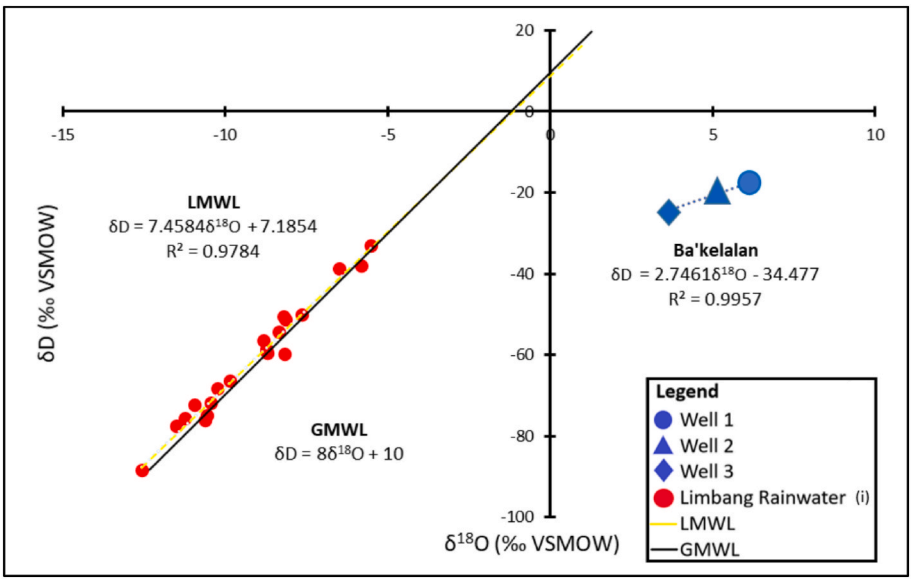

Fig. 5. δD versus $\delta^{18}O$ of Ba'kelalan groundwater samples compared with the LMWL (after (i) Ninu Krishnan et al., 2019) and GWML.

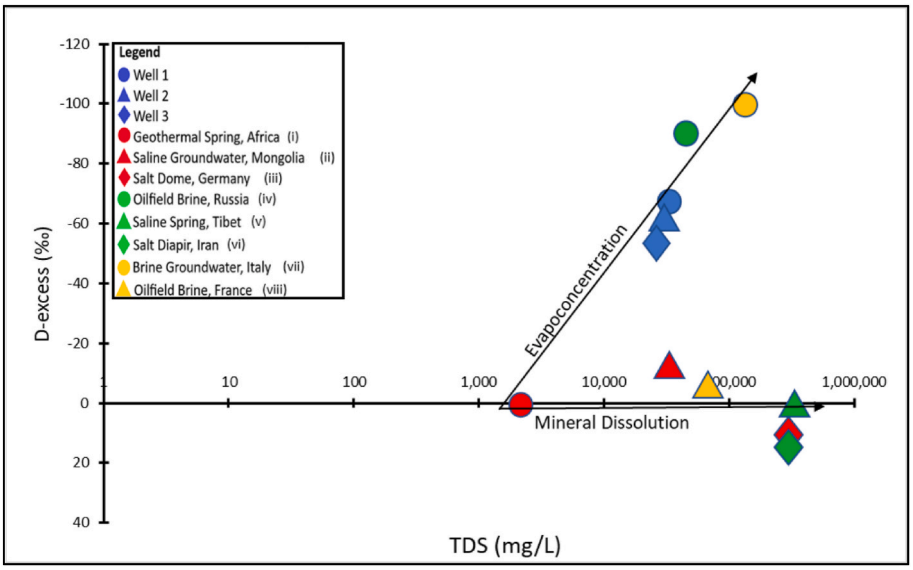

Fig. 6. D-excess versus TDS is plotted to identify the evaporation process in Ba'kelalan groundwater (after (i) Awaleh et al., 2020; (ii) Liu et al., 2016, (iii) Kloppmann et al., 2001; (iv) Shouakar-Stash et al., 2007; (v) Han et al., 2018; (vi) Bagheri et al., 2014a; (vii) Boschetti et al., 2011; (viii) Fontes and Mantray, 1993).

the TDS, EC and salinity values were recorded as the highest in well 1 and 2, followed by well 3 > well 4.

The physical parameter measurements for saline groundwater collected from 11th December 2018 to 24th January 2019, illustrated a significant increase in TDS, EC, and salinity for all the wells. This is due to the change from MON season to POM season, with various recharge resulted in the increased EC, TDS, and salinity values. The significant increase in EC and salinity in the groundwater is perhaps due to the seasonal change with the dilution effect from the recharge in this region (Mattos et al., 2018b). Large variations of TDS and EC values are majorly attributed to geochemical processes such as ion exchange, evaporation, mineral dissolution and rainwater infiltration (Ehya and Marbouti, 2016; Aghazadeh et al., 2017). The physical parameter values showed an increasing to decreasing concentration in TDS, EC and salinity values with a trend along the topography gradient from downstream to upstream: well 1 (913 m) > well 2 (913 m) > well 3 (914 m) > well 5 (948 m) > well 4 (967 m). Based on TDS values, well 1, 2, 3, 4 and 5 are classified as saline water (10,000–100,000 mg/L) and well 1, 2 and 3 are classified as brine water (<45,000 μS/cm). Meanwhile, well 4 and 5 are represented as saline water (2,000–45,000 μS/cm) based on EC values.

5.2. Hydrogeochemical processes

The Piper diagram (Fig. 11) shows that the chemical composition of the saline groundwater can be classified as Na^+- Cl^- water type for both seasons. Na^+- Cl^- facies generally indicate the characteristic of discharge zone, ion exchange process or the longer residence time of water in rock matrix (Piper, 1944; Devaraj et al., 2018; Mosaad and Kehew, 2019; Sivakarun et al., 2020). Based on the Durov diagram (Fig. 11), the trend for all the groundwater samples can be classified as Na^+ and Cl^- being the dominant anion and cation, which indicates that ion exchange is the dominant process in groundwater (Durov, 1948; Lloyd and Heathcote, 1985; Mosaad and Kehew, 2019).

Gibbs diagram (Gibbs, 1970) shows that all saline groundwater sample fall on evaporation dominance (Fig. 12). POM samples illustrate a higher ionic concentration (evapo-concentrates) from monsoonal

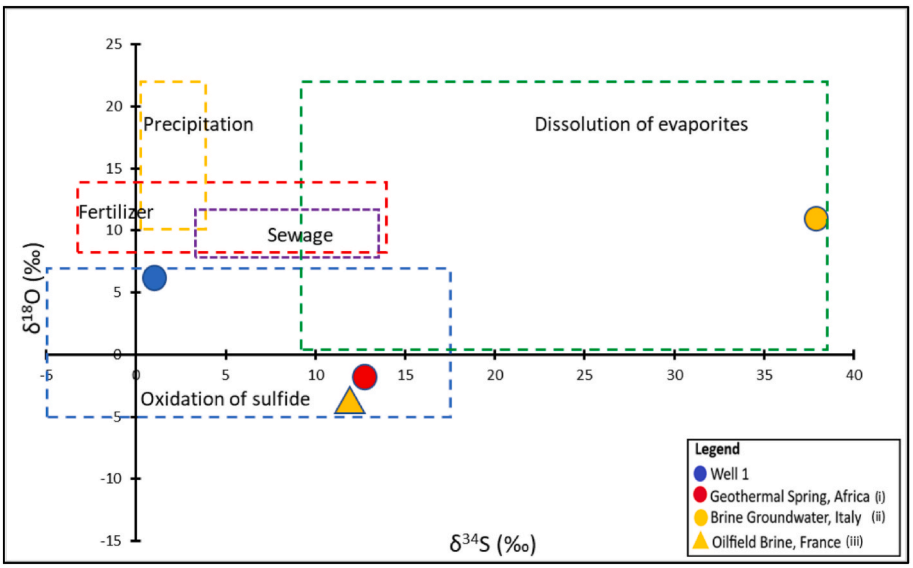

Fig. 7. The plot of $\delta^{34}S$ versus $\delta^{18}O$ by comparing with other related studies to identify the sources of Ba'kelalan groundwater (after (i) Awaleh et al., 2020; (ii) Boschetti et al., 2011; (iii) Fontes and Mantray, 1993).

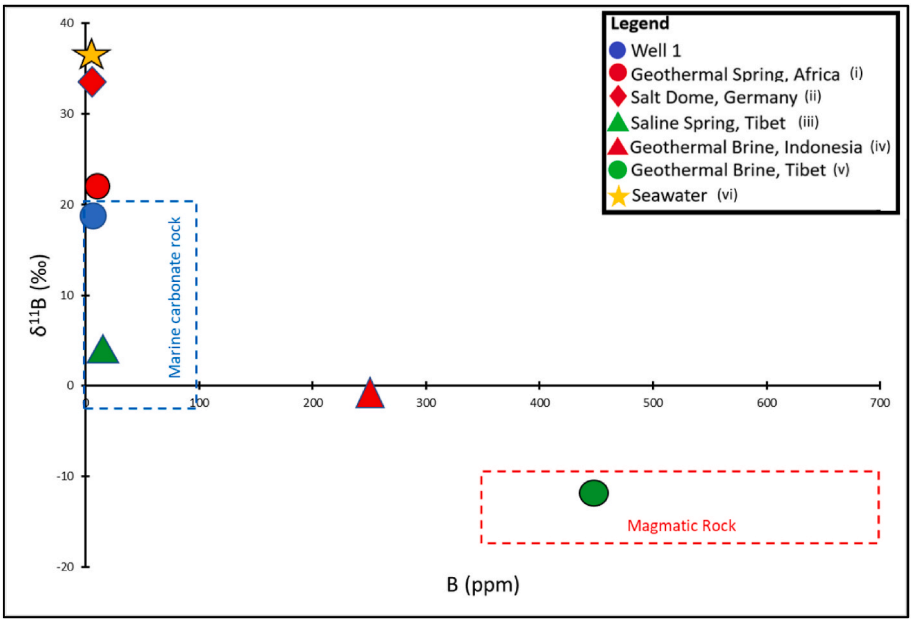

Fig. 8. The plot of $\delta^{11}B$ versus B by comparing with other related studies to identify the geogenic source of Ba'kelalan groundwater (after (i) Awaleh et al., 2020, (ii) Kloppmann et al., 2001; (iii) Han et al., 2018; (iv) Purnomo et al., 2016; (v) Liu et al., 2014; (vi) Drever, 1988).

recharge in which the plot shifts to the upper right. This indicates the potential dissolution of deposited evaporites in adjacent or underlying deeper aquifers (Haile, 1962). The groundwater is influenced by the dissolution of evaporite minerals due to the infiltration of monsoonal rainwater, whereby the processes might occur from the deeper aquifer with the help of fault or fracture for the passage of saline groundwater to the surface wells or springs (Liu et al., 2016; Marandi and Shand, 2018). Meanwhile, the Na^+/Cl^- versus EC plot (Fig. 13) shows a horizontal trend which indicates that the dissolution of evaporites might be the major process in controlling the chemistry of the groundwater in the study area, whereas the Na^+/Cl^- ratio almost remained unchanged (Jankowski and Acworth, 1997). The dissolution of evaporite minerals such as halite is in the deeper confined aquifer and was channeled to the unconfined zone or spring (Haile, 1962; Aquilano et al., 2016).

During MON, Na^+/Cl^- ratio is observed to have less ionic concentration due to more dilution compared to the POM season, indicating more ionic concentration due to the intense mineral dissolution during water-rock interaction (Fig. 13). The variation of Na^+/Cl^- ratio less than 1 is an indicator of depletion of Na^+ ions and can be attributed to reverse ion exchange, leading to Na^+ adsorption on clay minerals, and simultaneously releasing Ca^{2+} in groundwater (Mejri et al., 2018). Besides, a high concentration of Cl^- may originate from the dissolution of chloride-rich minerals such as halite or connate marine water entrapped in sediments (Zaidi et al., 2015; Ammar et al., 2020). This suggests that the source of salt is likely to be dominated by the dissolution of halite, as supported by the XRD data and other geochemical processes that should be responsible for the deviation from the 1:1 dissolution line (Kloppmann et al., 2001; Karakaya et al., 2019; Chander et al., 2020).

The plot of HCO_3^-/Na^+ versus Ca^{2+}/Na^+ (Fig. 13) shows the dissolution of evaporites as a major hydrogeochemical process for all the

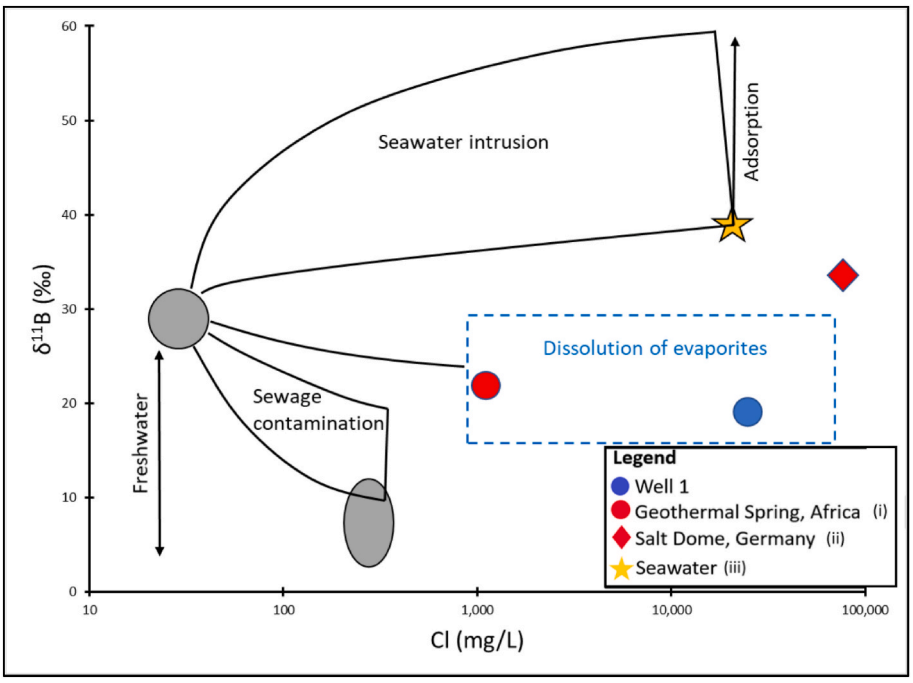

Fig. 9. The plot of $\delta^{11}B$ versus Cl by comparing with other related studies to identify the groundwater source of Ba'kelalan (after (i) Awaleh et al., 2020; (ii) Kloppmann et al., 2001; (iii) Drever, 1988).

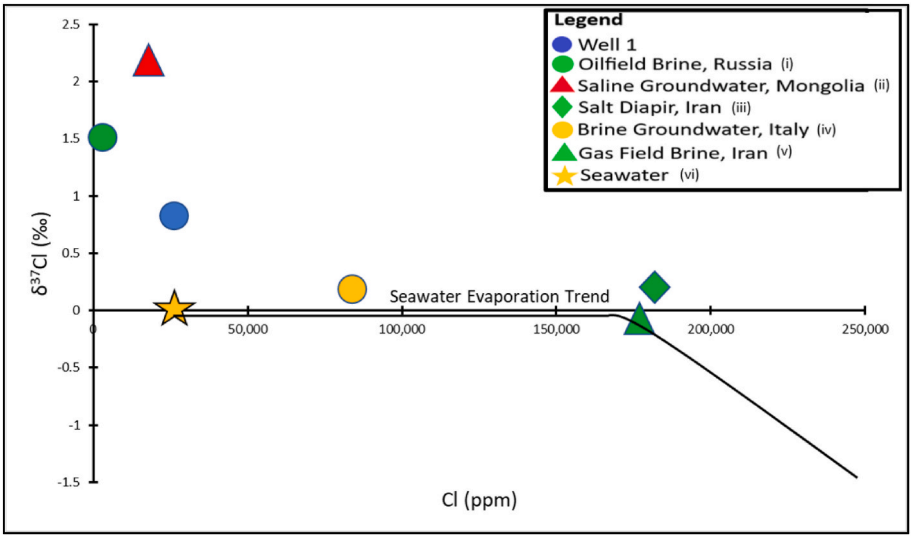

Fig. 10. The plot of $\delta^{37}Cl$ versus Cl by comparing with other related studies to identify the evaporation trend in Ba'kelalan groundwater (after (i) Shouakar-Stash et al., 2007; (ii) Liu et al., 2016; (iii) Bagheri et al., 2014a; (iv) Boschetti et al., 2011; (v) Bagheri et al., 2014b; (vi) Drever, 1988).

groundwater samples, probably in the deeper reservoir (Bozau et al., 2015; Fakharian and Narany, 2016). Thus, the MON season samples showed the influence of evaporite minerals with high rainfall, indicating water-rock interaction processes. Whereas, the POM season shows a more intense evaporation process compared to the MON season.

The positive value of CAI 1 and CAI 2 for groundwater sample indicates a reverse ion exchange process for both seasons (Fig. 14). Thus, the plot of $Ca^{2+} + Mg^{2+}$ versus $SO_4^{2-} + HCO_3^-$ shows that all the saline groundwater samples for the MON fall above the 1:1 line (Fig. 14), indicating an excessive of Ca^{2+} and Mg^{2+} originated from other processes such as reverse ion exchange (Zaidi et al., 2015). Whereas, the POM samples are scattered close and below the 1:1 dissolution line, indicating an excess of $SO_4^{2-} + HCO_3^-$ that can be attributed to the ion exchange process or dissolution of gypsum, calcite and dolomite (Sheikhy Narany et al., 2014; Duan et al., 2022).

Based on the Brine Differentiation plot and Langlier-Ludwig diagram (Fig. 15) (Langelier and Ludwig, 1942; Hounslow, 1995), the saline groundwater samples fall on the Na^+- Cl^- brine zone for POM season, indicating the longer residence time of water in a deeper condition that has resulted in the dissolution of evaporite minerals, leading to higher salinity content (Boschetti et al., 2016; Awaleh et al., 2020). Whereas, the MON samples are more shifted towards Ca^{2+}- Cl^- oil field brine zone (Özdemir, 2018).

5.3. Saturation index

The SI versus HCO_3^- in the MON season shows that the carbonate minerals (aragonite, dolomite and calcite) are between saturated and

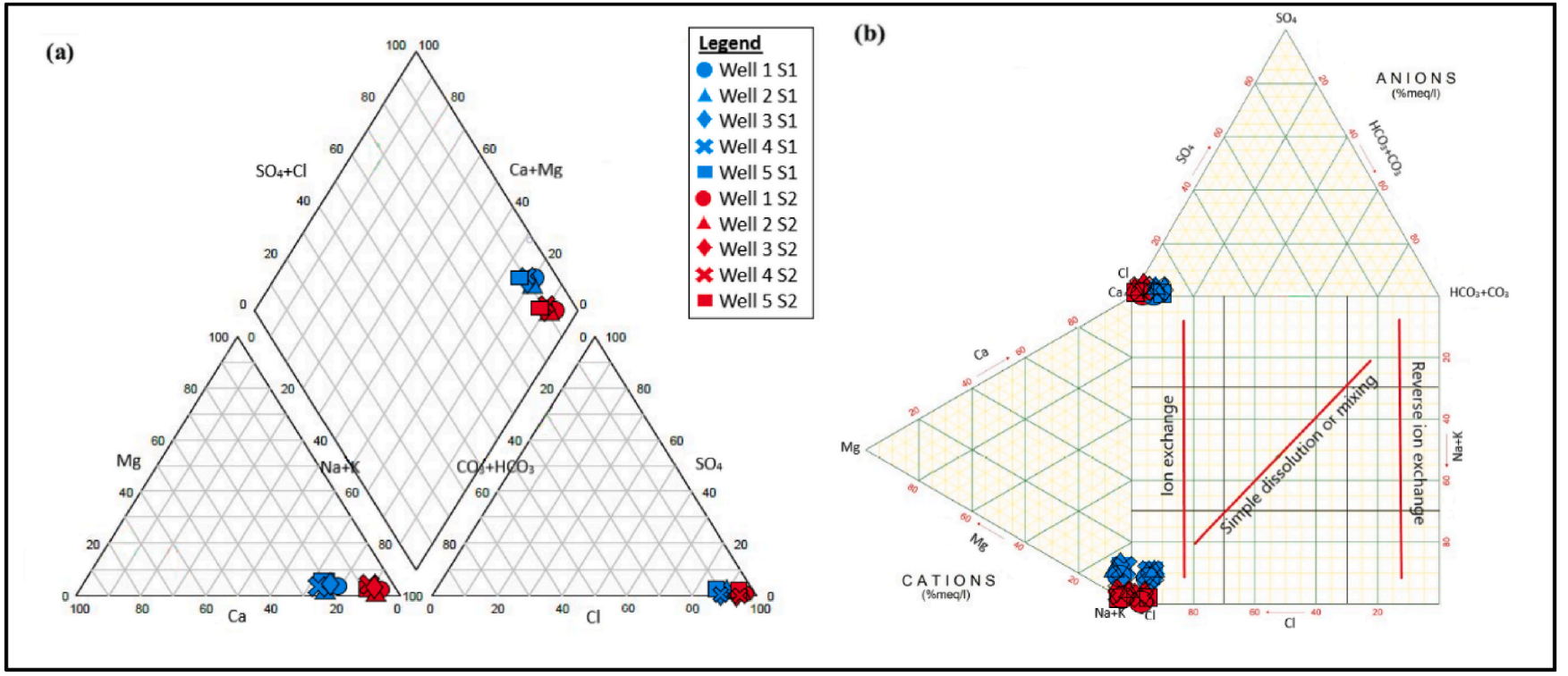

Fig. 11. (a) Piper diagram and (b) Durov diagram for Ba'kelalan saline groundwater to identify the water types and its related geochemical processes.

oversaturated irrespective of seasons, whereas, for the POM season, these minerals tend to form a more saturated state, probably due to less recharge and precipitation (Fig. 16). The pH showed a slight increase in the saturation trend with increasing pH value for both MON and POM seasons (dolomite, aragonite and calcite), indicating that the minerals were precipitated in a higher pH condition. Magnesite and barite were undersaturated and close to an equilibrium state (SI = 0) for both seasons, however, the SI of minerals for halite, anhydrite and gypsum were shown to be undersaturated. The SI for halite dissolution showed a distinct difference between MON (−3 to −4) with more dissolution, while POM (−2 to −3) has comparatively less dissolution.

5.4. Isotopic signatures

The $\delta^{18}O$ and δD values show that well 1 sample is more enriched in $\delta^{18}O$ concentration compared to well 2 and well 3. The slope of GMWL and LMWL is close to each other due to the local climatic factors including air, temperature, evaporation, seasonal precipitation and moisture source (Thivya et al., 2016; Gautam et al., 2017; Lyu et al., 2019; Dişli and Gülyüz, 2020; Ninu Krishnan et al., 2022). The analysed saline groundwater samples plotted away from the GMWL and the LMWL with an enrichment isotopic concentration of $\delta^{18}O$ indicate that the meteoric water was not the main origin of the groundwater recharge in the study area (Coplen, 1994; Boschetti et al., 2016). The saline groundwater enriched value in $\delta^{18}O$ could be mainly due to the evaporation process, witnessed in the Gibbs plot and other geochemical plots. The enrichment in $\delta^{18}O$ of the groundwater may be due to a variety of processes, such as water-rock interaction, ancient seawater evaporation or mineral dehydration. The negative δD values can be an indicator of ion hydration effects of mineral dissolution such as halite, as witnessed by XRD data of salt sample or isotope exchange during hydration and dehydration of minerals (McHenry et al., 2020). The saline groundwater sample trend line intersects the LMWL at a particular point, suggesting that the interconnection by a particular location and period might be the source of local precipitation (Liu et al., 2016). This suggests that the recharge might have occurred during January 2017 at Kampong Salidong, Limbang, Sarawak (Ninu Krishnan et al., 2022).

The groundwater samples' d-excess values are negative and very low, indicating that values less than 3‰ is revealed the source as evaporative enrichment with certainty (Dansgaard, 1964; Thivya et al., 2016). The increasing trend in TDS with a decrease in d-excess (Fig. 6), suggesting that an intense evaporation process occurred in the deeper aquifer (Dansgaard, 1964; Evans et al., 2015; Ninu Krishnan et al., 2019; Torres-Martínez et al., 2020). The $\delta^{34}S$ in the groundwater was close to oxidative weathering of metamorphic pyrite with a value of – 1.8 to 2.4‰ (Tostevin et al., 2016; Lyu et al., 2019). The $\delta^{34}S$ has a value fall on the oxidation sulfide zone, indicating oxidization by pyrite concentration as witnessed in geochemical plots, and pyrite grains are identified through visual identification and XRD data of the salt sample (Tostevin et al., 2016; Wang and Zhang, 2019). The following equation explains the chemical reaction for pyrite oxidation:

$$2FeS_2 + 7O_2 + 2H_2O \rightarrow 2Fe^{2+} + 4SO_4^{2-} + 4H^+ \quad (4)$$

The saline groundwater sample has a $\delta^{11}B$ value of 18.2‰, which fall on dissolution of marine carbonate rocks zone. Hence, the dissolution of marine evaporites at the deeper circulation of groundwater through the infiltration of monsoonal rainwater, which is reflected by $\delta^{11}B$ value (Purnomo et al., 2016; Du et al., 2019; Ercan et al., 2019). The saline groundwater sample has a $\delta^{37}Cl$ value of 0.82‰, indicating that halite dissolution could be the major process affecting the salinization in the study area (Sherif et al., 2019) which is justified by the XRD data of the salt sample (Birks et al., 2019). It is interesting to observe that the enrichment of $\delta^{37}Cl$ was around 25,000 ppm of Cl^- concentration, which also indicating the intense evaporation process in the deeper circulation of groundwater.

5.5. Statistic analysis of saline groundwater

The results of principal component analysis (PCA) and factor scores are presented in Table 2. For the factor loadings, high loading is defined as greater than 0.75, moderate loading as 0.50–0.75, and a loading with less than 0.50 is considered insignificant (Ibrahim et al., 2019). Principal component analysis for the MON season showed that four factors (PC1, PC2, PC3 and PC4) explained 43.5, 34.8, 14.3 and 7.3% respectively of the total variance. PC1 has the highest factor loadings for major ions (Na^+, Cl^- and HCO_3^-), nutrients (PO_4^{3-} and P) and physical parameters, indicating that TDS, EC and salinity are mainly controlled by these elements and most likely to be derived from the same source. The high factor loading of Na^+, Cl^-, TDS and EC in this factor, suggesting the most important role of these two ions (Na^+ and Cl^-) in the salinization or

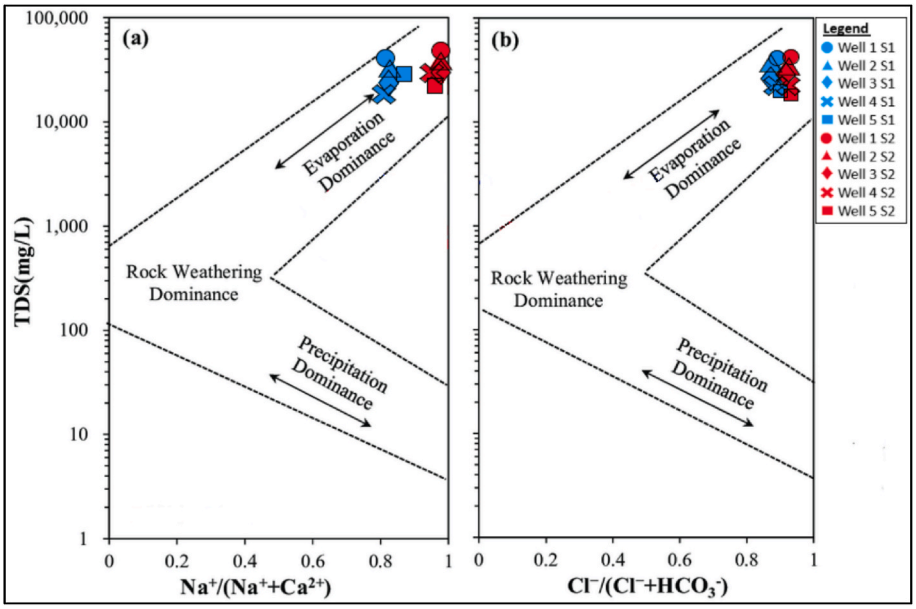

Fig. 12. Gibbs diagram to identify the major hydrogeochemical processes in the study area.

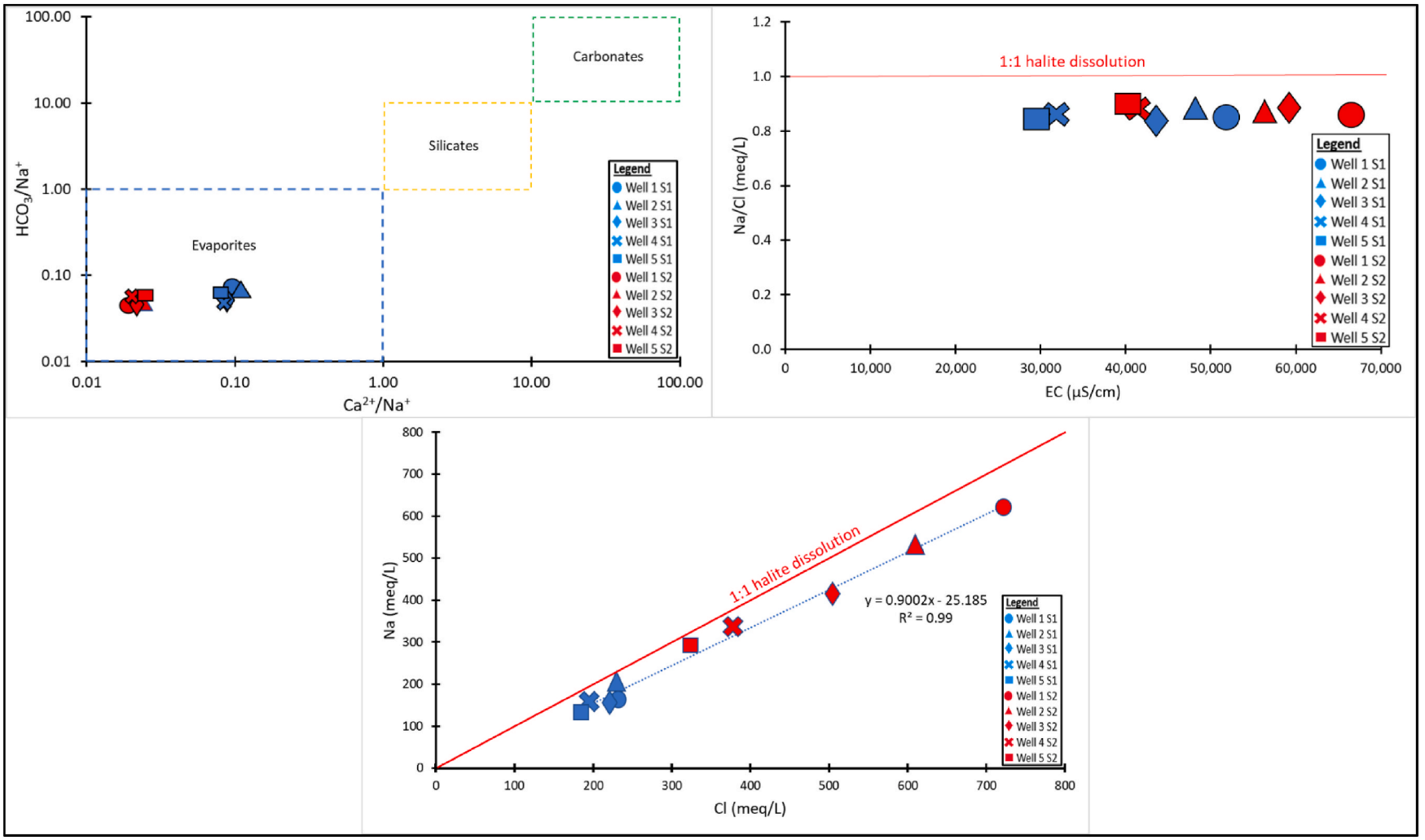

Fig. 13. Ionic ratio plots to depicts the major hydrogeochemical processes in the study area.

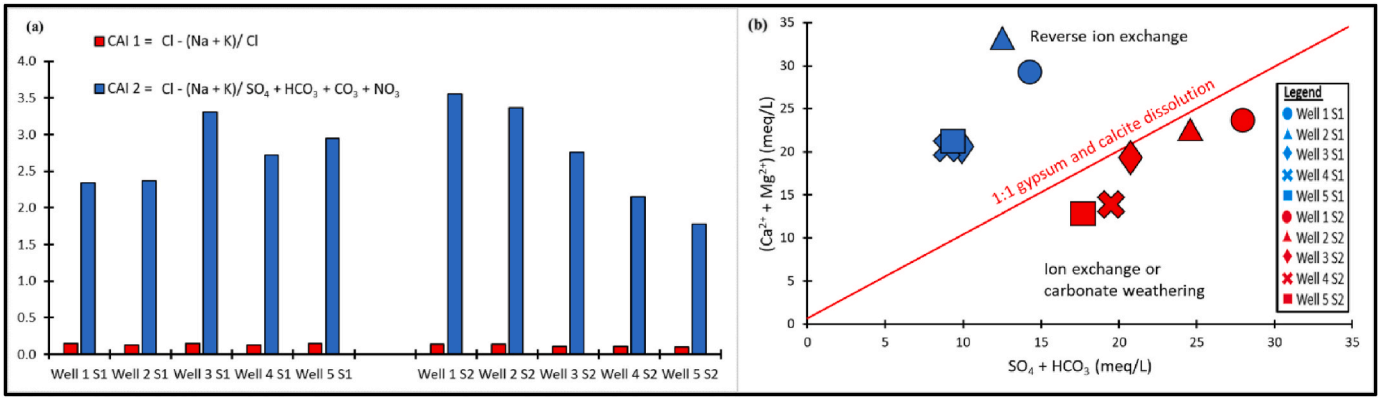

Fig. 14. (a) Chloro Alkali Indices and (b) ionic ratio plot to identify weathering and ion exchange processes.

mineralization process. High loading of Rb, B and Li indicates a common source such as clays or shale (Han et al., 2018). Besides, the level of salinity of the groundwater has influenced the concentration and mobility of these trace metals (Jia et al., 2017; Esmaeili et al., 2018). Meanwhile, the high negative loadings of temperature, K^+, Mn, Br, Co, Cd and Sn, indicated that temperature plays a significant role in controlling these metals (Belkhiri et al., 2017). From the factor score, well 1 has contributed more (+) in this factor. The PC2 is mainly controlled by the positive loadings of PO_4^{3-}, P, K^+, Ca^{2+}, Mg^{2+}, HCO_3^- and Sc, and represents in well 1. This may indicate that P and PO_4^{3-} are associated with Sc which may be due to leaching or dissolution from common source rocks such as shale or mudstone (Oyem et al., 2017). On the other hand, PC3 is less defined, which explains 14.3% of the variability of data for well 2. The highest loading is shown by the turbidity, NH_4, NH_3, NH_3N, SO_4^{2-}, Ca^{2+}, Fe, Cd and Cu, indicating that the association of Fe, Cu and Cd is probably dependent on the availability of nutrients present in the groundwater and commonly found in pyrite and chalcopyrite in an oxygen-poor environment (Samantara et al., 2017). The turbidity of the groundwater samples plays an essential role in controlling most of the nutrients, especially SO_4^{2-} and is associated with Fe. Organic matter, iron (Fe^2) and pyrite (FeS_2) are important substitution donors for nitrate reduction (Kaown et al., 2020; Torres-Martínez et al., 2020). In PC4, temperature indicated the role in controlling the mobility of Mn, Sc, Co and Cr in the groundwater (Samantara et al., 2017), which results in well 5 with the lowest variance.

PCA for the POM season is represented by four factors (PC1, PC2, PC3 and PC4) explaining 60.9, 22.01, 11.56 and 5.49% of the total variance respectively (Supplementary Table 2). PC1 shows the highest positive loading with 60.9% of variability for the physical parameters (TDS, EC, salinity and temperature), major ions (Na^+, Cl^-, Ca^{2+}, Mg^{2+} and HCO_3^-), nutrient (NH_4, NH_3 and NH_3N) and trace metals (Cd, Cu, Rb, B and Li). The samples with high contribution to PC1 are from well 1, indicating a progression of mineralization towards the high salinization processes in groundwater, which is the Na^+- Cl^- water type. It has the highest positive loadings for most variables, especially Na^+, Cl^-, TDS and EC, which may indicate salinization by mineral dissolution. Besides, the high loading for Na^+, Mg^{2+} and Ca^{2+} indicate potential ion-exchange processes (Zaidi et al., 2015; Ibrahim et al., 2019). Furthermore, the temperature indicated the role of controlling the trace metals' (Cd, Cu, Rb, B and Li) mobility in the groundwater (Madzin et al., 2017; Akoto et al., 2019). The strong factor loading of Cd, Rb, Cu, B and Li indicate possible common source such as clay, shale or sulphide mineral-like pyrite (Tostevin et al., 2016). Whereas, pH showed high negative loading with Fe, Ba, Cr and Sn, indicating that the acidic pH has released these trace metals in groundwater (Esmaeili et al., 2018). The PC2 is represented by the moderate factor loadings of temperature, K^+, Ca^{2+}, nutrients (SO_4^{2-}, NH_4, NH_3 and NH_3N) and trace metals (Sc, Rb, B and Li), which is mostly contributed in well 2. Similarly, with PC1, the temperature played an essential role in the mobility of trace metals (Sc, Rb, B and Li) in the groundwater. Whereas, the nutrients are controlled by Ca^{2+} and K^+ in the groundwater. For PC3, the turbidity, nutrients (PO_4^{3-}, P, NO_3^- and NO_2^-) and trace metals (Zn and Rb) suggested that the groundwater turbidity depends on the concentration of the nutrients (PO_4^{3-}, P, NO_3^- and NO_2^-) and trace metals. The PC4 shows that the NH_3 and NH_3N are related to the Fe, indicating the reducing environment, which has controlled these elements in the groundwater.

5.6. Correlation of 2D resistivity and seismic refraction in 3D display

The 2D resistivity method suggests that the lowest resistivity value of 0.2 Ω m – 2.84 Ω m reflects the presence of the saline groundwater adjoining the existing well sites besides indicating the presence of a perched aquifer (Mainoo et al., 2019). The lowest resistivity values were observed in nearby perched aquifer (spring) with a value of 2.8 to < 10 Ω m at a depth of 1–14 m, suggest the saline groundwater, as changes in salinity lead to changes in resistivity (Mahmoud and Ghoubachi, 2017). The resistivity value of ≈60 Ω m suggests a sandy layer or saturated layer (Islami et al., 2018), and the resistivity value of 115 Ω m – 505 Ω m indicates the weathered topsoil layer (Farid et al., 2017). The movement of the groundwater plume is indicated by the flow from higher to lower elevation (NW to SE) due to the hydraulic pressure gradient, where the saline groundwater moved or upwelled to the surface as spring. Whereby the perched water table is intersected the ground surface in the middle of the section.

The seismic refraction determined that the first layer velocity ranges between 209 m/s and 991 m/s, indicating the unconsolidated weathered topsoil layer (Araffa et al., 2017). The second layer velocity ranges between 1329 and 2579 m/s, and reflects the saturated layer of saline groundwater at a depth of approximately 5 m (Jagadeshan et al., 2018; Azhar et al., 2019). The velocity of the third layer ranges from 2718 to 3370 m/s reflecting a partial saturated layer which could be a clayey sandy layer or shale layer (Desper et al., 2015; Oskooi et al., 2019). Faults has been detected in most of the survey profiles at approximate depth of 10 m with a rapid lateral change of velocity (down thrown zone) (Al-Heety, 2018).

The 3D profiles are displayed by combining the 2D resistivity and seismic refraction images separately (Fig. 17) from 3 survey profiles in the study area. These 3D profiles provide a clearer image of the subsurface and help in a better understanding of the groundwater flow and structures. In Fig. 17, the 3D profile of the 2D resistivity profile consisted of profiles R1, R2 and R3 as the main target perched aquifer. The image confirms that the groundwater was at the depth of 2–15 m below the surface, whereas the groundwater plume flowed from SW to NE direction. Due to the hydraulic pressure gradient of the saline groundwater

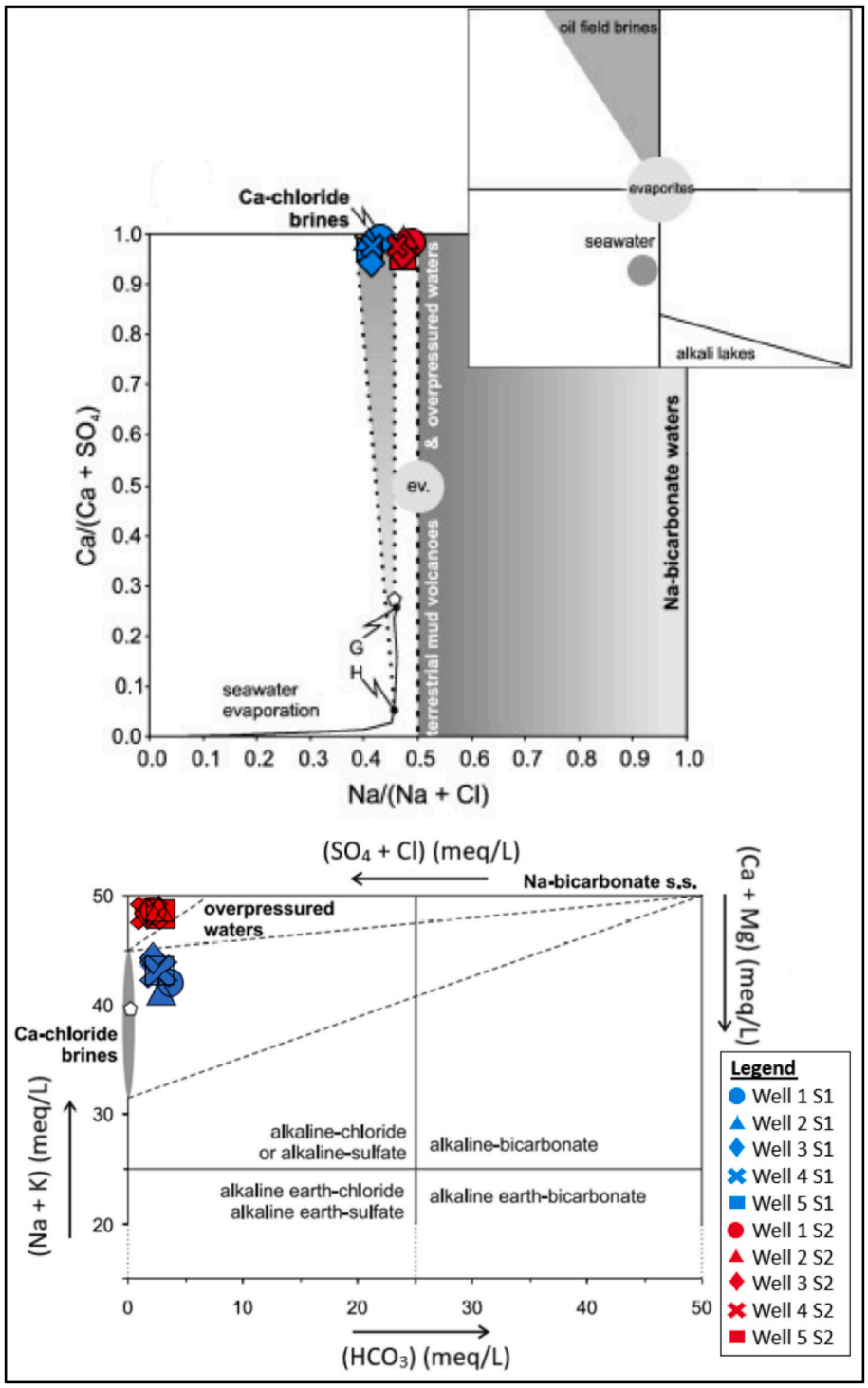

Fig. 15. Brine Differentiation and Langlier-Ludwig plots to depict the origin of groundwater.

that has moved from a higher elevation from NW to SE and an upwelling (anticlinal structure) to the surface facilitating the perched water table to discharge at the ground surface. Fig. 17 shows the faults based on the rapid lateral change in velocity of the second and third zone, and are marked in black circle. This rapid lateral change in velocity can be interpreted as a local fault (Al-Heety, 2018). The localized fault profile 1 has been detected at a distance of 30 m towards NW and 90 m towards the SE direction (Supplementary Fig. 2). Profile 2 is at a distance of 75 m dipping NW and 95 m dipping SE, thus, both profiles show graben fault structure due to depression with the fact that it is in a valley (Supplementary Fig.3). For profile R3, the fault is located at the perched aquifer at 75 m marked, illustrating a normal fault structure (Supplementary Fig. 4). The presence of faults near the perched aquifer has facilitated the groundwater movement from the saturated zone to the surface. Thus, it is clear that the perched aquifer has the potential to provide a sufficient supply of saline groundwater for future drilling sites in the study area.

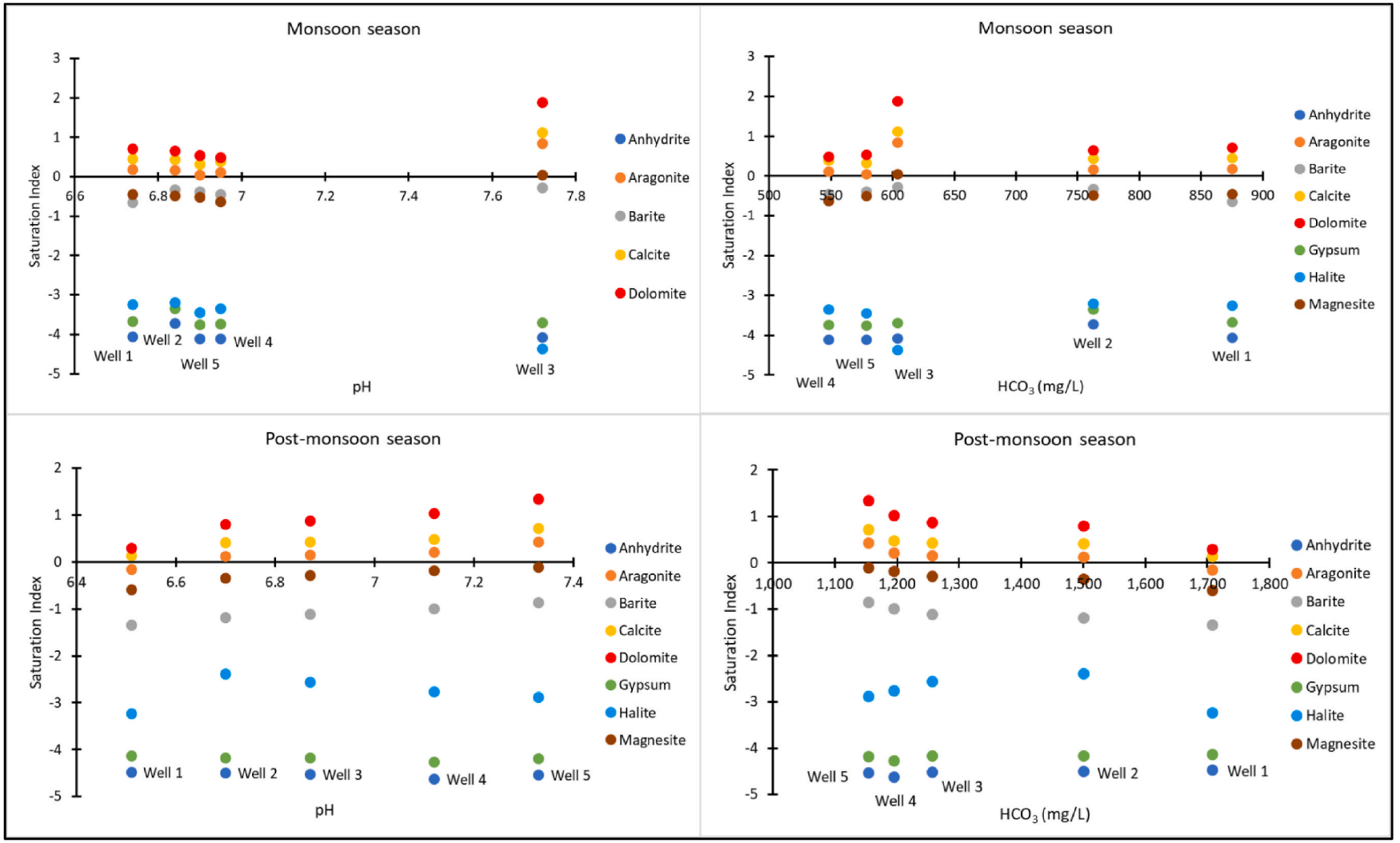

Fig. 16. Saturation Index of carbonate and sulphate minerals during MON and POM periods.

Table 2
The results of principal component analysis (PCA) and factor scores from the geochemical data for (a) monsoon and (b) post monsoon seasons.

Rotated Component Matrix					Rotated Component Matrix				
a) MON	1	2	3	4	**b) POM**	1	2	3	4
pH	**.098**	**−.924**	−.369	−.001	pH	**−.938**	−.345	−.004	.021
Temperature	**−.691**	.101	−.031	**.715**	Temperature	**.655**	**.583**	−.441	.190
TDS	**.961**	.155	.058	−.223	TDS	**.941**	.262	.195	−.087
EC	**.963**	.146	.057	−.217	EC	**.945**	.163	−.242	−.146
Salinity	**.963**	.160	.057	−.207	Salinity	**.927**	.293	−.167	.164
Turbidity	.093	.166	**.980**	−.056	Turbidity	.151	−.102	**.979**	.093
SO_4^{2-}	.339	.063	**.937**	−.053	SO_4^{2-}	.010	**.986**	.073	−.149
PO_4^{2-}	**.521**	**.816**	.035	−.248	PO_4^{2-}	.346	.255	**.894**	.127
P	**.541**	**.806**	.033	−.238	P	.358	.192	**.891**	−.203
NO_3^-	.350	**−.882**	−.316	.008	NO_3^-	−.309	−.169	**.927**	.130
NO_2^-	.350	**−.882**	−.315	.009	NO_2^-	−.330	−.156	**.922**	.132
NH_4^+	−.204	.266	**.942**	−.012	NH_4^+	**.658**	**.531**	.237	.479
NH_3	−.205	.265	**.942**	−.013	NH_3	**.610**	**.550**	.188	**.539**
NH_3N	−.198	.277	**.940**	−.019	NH_3N	**.585**	**.552**	.119	**.582**
Na^+	.908	.042	.178	−.378	Na^+	**.903**	.393	−.067	.160
K^+	−.705	**.530**	.449	−.141	K^+	.442	**.850**	.247	.147
Ca^{2+}	.497	**.616**	**.560**	−.245	Ca^{2+}	**.778**	**.560**	−.263	−.114
Mg^{2+}	.390	**.760**	.493	.165	Mg^{2+}	**.946**	.323	−.003	−.038
Cl^-	**.952**	.011	.094	−.291	Cl^-	**.923**	.367	−.087	.078
HCO_3^-	**.814**	**.569**	.101	−.057	HCO_3^-	**.889**	.372	−.003	.266
Mn	−.496	.129	−.047	**.857**	Mn	.123	**−.632**	**−.765**	−.001
Fe	.414	.264	**.871**	−.016	Fe	**−.690**	.044	−.459	**.557**
Ba	**−.814**	−.438	−.054	.377	Ba	**−.976**	.094	−.055	−.188
Zn	−.044	**−.954**	−.251	−.158	Zn	−.361	.071	**.828**	−.422
Sc	.074	**.582**	**−.521**	**.621**	Sc	.129	**.953**	.017	.275
Co	**−.519**	.036	−.018	**.854**	Co	**−.748**	−.653	−.003	−.116
Cd	−.173	.083	**.823**	−.535	Cd	**.792**	−.019	.464	.397
Cu	**−.786**	.166	**.582**	−.125	Cu	**.974**	−.054	−.045	.217
Cr	−.287	−.321	−.154	**.890**	Cr	**−.527**	**−.849**	.036	−.013
Rb	**.814**	**−.564**	−.119	−.075	Rb	**.545**	**.599**	**.557**	−.184
Sn	**−.890**	−.339	−.027	.304	Sn	**−.872**	−.447	−.174	.095
B	**.892**	−.406	−.176	−.094	B	**.711**	**.595**	−.375	−.002
Li	**.903**	−.379	−.193	−.060	Li	**.551**	**.696**	−.457	.060
Factor Scores	**F1**	**F2**	**F3**	**F4**	**Factor Scores**	**F1**	**F2**	**F3**	**F4**
Well 1	**0.96**	**1.18**	**−0.92**	−0.19	Well 1	**1.43**	−0.30	−0.25	**1.01**
Well 2	0.61	0.11	**1.68**	−0.09	Well 2	0.02	**1.76**	0.13	−0.27
Well 3	0.58	**−1.59**	−0.58	0.02	Well 3	0.33	**−0.66**	−0.46	**−1.57**
Well 4	**−1.26**	0.07	−0.10	**−1.27**	Well 4	−0.50	−0.54	**1.62**	0.16
Well 5	−0.89	0.23	−0.08	**1.53**	Well 5	**−1.27**	−0.26	**−1.04**	0.66

*bolded text indicates significant loading.

6. Conclusion

In this study, the potential sources, hydrogeochemistry, lithology and structural controls of saline groundwater in Ba'kelalan region was investigated and the observations derived from the study are summarised as follows;

- The study infers that there is an increase in salinity of groundwater with respect to seasons that affects the amount of salt production, where hourly and daily observation of water level fluctuation reflects the changes in groundwater recharge.
- The groundwater samples are classified as Na–Cl type and dominated by the dissolution of evaporites. The reverse ion exchange process is inferred to occur in MON season, whereas the ion exchange and carbonate dissolution are predominant processes in POM season.
- Enriched $\delta^{18}O$, δD and low d-excess values of groundwater samples indicate the origin of the saline groundwater is from a high intense evaporation water source.
- $\delta^{37}Cl$, $\delta^{11}B$ and $\delta^{34}S$ in groundwater samples indicated halite dissolution, marine evaporite dissolution and oxidation of sulphide (pyrite), which is also witnessed in the visual identification of rock sample and XRD data of salt sample.
- Based on the results of the geochemical and geophysical studies, the source of the existing well water is mainly due to the dissolution of evaporites and they are connected through a fault system reaching the shallow levels. The perched aquifer in the study area was connected to the deeper aquifer by fractures and faults with a capacity and to provide copious saline water supply even during the dry season. Therefore, the perched aquifer is the most suitable and possesses a promising location for utilisation of saline water to manufacture high mountain salt.
- The saline groundwater chemistry provided knowledge on the saline groundwater characteristics, and this can be used for agricultural purposes, especially for high salinity tolerant crops in the near future.
- This study tries to address SDG 6 (Clean water and Sanitation) with respect to the increased water use efficiency, integrated water resources management, and restoration water related ecosystems.
- Further involvement in the community-based water management system is crucial as this study is much needed by the community in improving their livelihood, while their participation in the study could assist in capacity building. Hence, the outcome of the study will form the baseline for the community's future development of mountain salt production.

Credit author statement

Stephan Ongetta – Formal analysis and Writing original draft

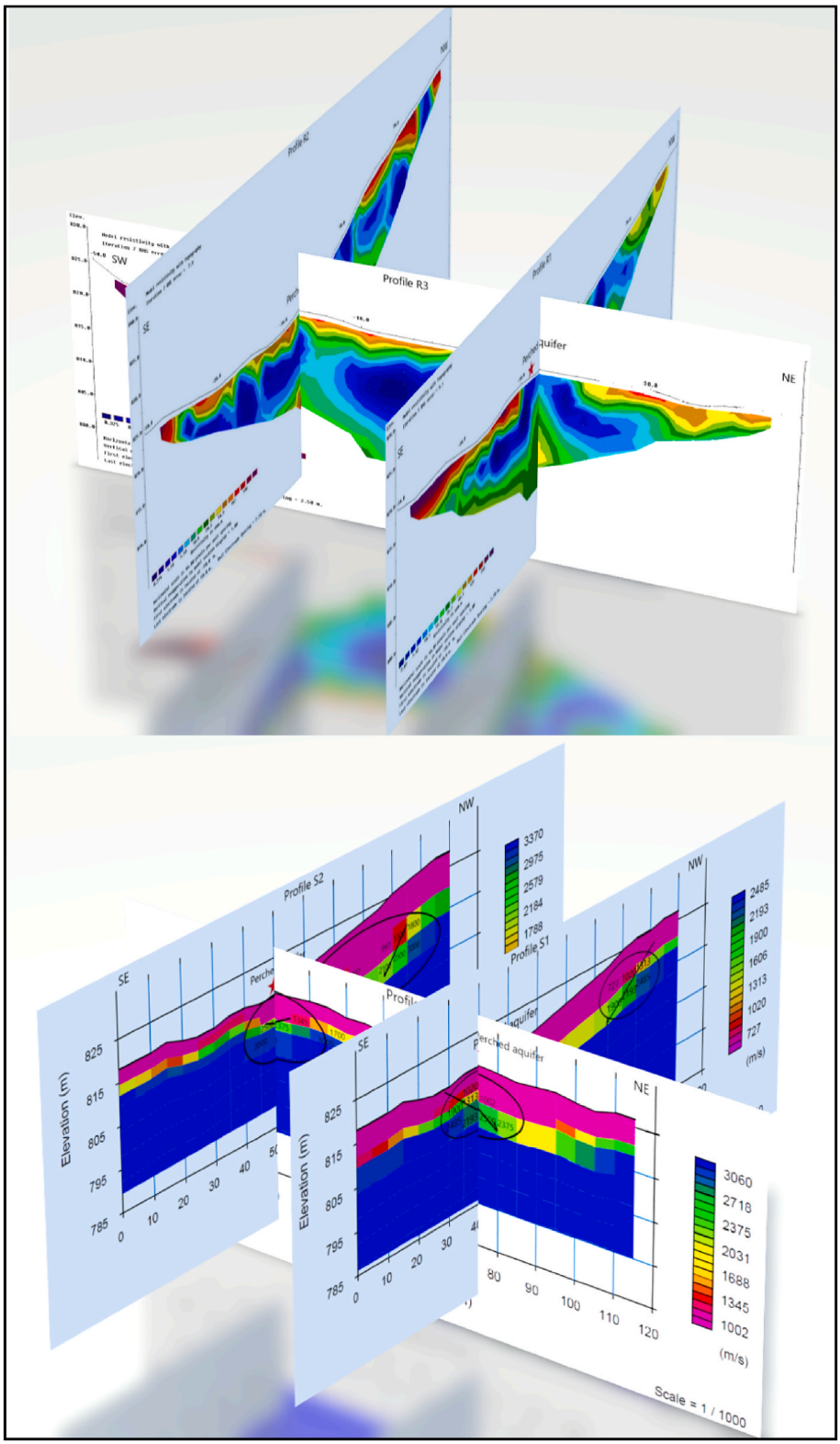

Fig. 17. 3D profile for 2D resistivity (R1, R2, R3) and seismic refraction (S1, S2, S3) to predict the aquifer connectivity and subsurface geological structures.

Prasanna – Investigation & Editing, Data curation, Project administration Chidambaram – Reviewing & Editing Nagarajan – Reviewing & Editing Clem Kuek – Conceptualization & Editing.

Declaration of competing interest

The authors declare that they have no known competing financial interests or personal relationships that could have appeared to influence the work reported in this paper.

Data availability

The data that has been used is confidential.

Acknowledgement

This research was fully funded by the Curtin Malaysia Research Institute (CMRI) and the first and second authors would like to thank the CMRI for providing a Scholarship (SO) and awarded a research grant to Dr. MVP. The authors are also thankful to UKM for the assistance in conducting the geophysical survey. Special thanks to Dr. Devaraj for helping with the graphical abstract.

Appendix A. Supplementary data

Supplementary data to this article can be found online at https://doi.org/10.1016/j.chemosphere.2022.135721.

References

Abdullah, W.H., Togunwa, O.S., Makeen, Y.M., Hakimi, M.H., Mustapha, K.A., Baharuddin, M.H., Tongkul, F., 2017. Hydrocarbon source potential of eocene-miocene sequence of western Sabah, Malaysia. Mar. Petrol. Geol. 83, 345–361. https://doi.org/10.1016/j.marpetgeo.2017.02.031.

Adithya, V.S., Chidambaram, S., Tirumalesh, K., Thivya, C., Thilagavathi, R., Venkatramanan, S., Prasanna, M.V., Dhanu, R.S., 2020. Seasonal changes in groundwater quality deterioration and chemometric analysis of pollution source identification in South India. Environ. Sci. Pollut. Control Ser. 27, 20037–20054 org/10.1007/s11356-020-08258-6.

Aghazadeh, N., Chitsazan, M., Golestan, Y., 2017. Hydrochemistry and quality assessment of groundwater in the Ardabil area, Iran. Appl. Water Sci. 7 (7), 3599–3616. https://doi.org/10.1007/s13201-016-0498-9.

Aizebeokhai, A.P., Oyeyemi, K.D., Joel, E.S., 2016. Groundwater potential assessment in a sedimentary terrain, Southwestern Nigeria. Arabian J. Geosci. 9 (7), 496. https://doi.org/10.1007/s12517-016-2524-5.

Akinbiyi, O.A., Oladunjoye, M.A., Sanuade, O.A., Oyedeji, O., 2019. Geophysical characterization and hydraulic properties of unconsolidated floodplain aquifer system in Wamako area, Sokoto State, Northwestern Nigeria. Appl. Water Sci. 9 (8), 177. https://doi.org/10.1007/s13201-019-1065-y.

Akoto, O., Teku, J.A., Gasinu, D., 2019. Chemical characteristics and health hazards of heavy metals in shallow groundwater: case study Anloga community, Volta Region, Ghana. Appl. Water Sci. 9 (2), 36. https://doi.org/10.1007/s13201-019-0914-z.

Al-Heety, A., 2018. An Evaluation between Time-Term, Reciprocal Time and Refraction Tomography Analysis Methods for Obtaining 2-D Shallow Seismic Velocity Models over Synthetic Travel Times. https://doi.org/10.31223/osf.io/gbqe6.

Alekseeva, L.P., Alekseev, S.V., 2018. Geochemistry of ground ice, saline groundwater, and brines in the cryoartesian basins of the Northeastern Siberian Platform. Russ. Geol. Geophys. 59 (2), 144–156. https://doi.org/10.1016/j.rgg.2018.01.012.

Alexeeva, S.V., Alexeeva, L.P., Vakhromeev, A.G., 2020. Brines of the Siberian platform (Russia): geochemistry and processing prospects. Appl. Geochem. https://doi.org/10.1016/j.apgeochem.2020.104588, 104588.

Alhassan, D.U., Obiora, D.N., Okeke, F.N., Ibuot, J.U., 2018. Investigation of groundwater potential of Southern Paiko, Northcentral Nigeria, using seismic refraction method. Model. Earth Syst. Environ. 4 (2), 555–564. https://doi.org/10.1007/s40808-018-0452-y.

Ammar, S.B., Taupin, J.D., Alaya, M.B., Zouari, K., Patris, N., Khouatmia, M., 2020. Using geochemical and isotopic tracers to characterize groundwater dynamics and salinity sources in the Wadi Guenniche coastal plain in Northern Tunisia. J. Arid Environ. 178, 104150 https://doi.org/10.1016/j.jaridenv.2020.104150.

Anomohanran, O., Ofomola, M.O., Okocha, F.O., 2017. Investigation of groundwater in parts of Ndokwa District in Nigeria using geophysical logging and electrical resistivity methods: implications for groundwater exploration. J. Afr. Earth Sci. 129, 108–116. https://doi.org/10.1016/j.jafrearsci.2016.12.008.

APHA, A., 1998. Standard Methods for the Examination of Water and Wastewater. American Public Health Association. Inc., Washington. DC.

Aquilano, D., Otálora, F., Pastero, L., García-Ruiz, J.M., 2016. Three study cases of growth morphology in minerals: halite, calcite and gypsum. Prog. Cryst. Growth Char. Mater. 62 (2), 227–251. https://doi.org/10.1016/j.pcrysgrow.2016.04.012.

Araffa, S.A.S., Mohamed, A.M., Santos, F.M., 2017. Geophysical investigation in the northwestern part of the Gulf of Suez, Egypt. Egypt. J. Petrol. 26 (2), 457–475. https://doi.org/10.1016/j.ejpe.2016.06.002.

Awaleh, M.O., Boschetti, T., Soubaneh, Y.D., Kim, Y., Baudron, P., Kawalieh, A.D., Adiyaman, Ö., 2018. Geochemical, multi-isotopic studies and geothermal potential evaluation of the complex Djibouti volcanic aquifer (Republic of Djibouti). Appl. Geochem. 97, 301–321. https://doi.org/10.1016/j.apgeochem.2018.07.019.

Awaleh, M.O., Boschetti, T., Adaneh, A.E., Daoud, M.A., Ahmed, M.M., Dabar, O.A., Kadieh, I.H., 2020. Hydrochemistry and multi-isotope study of the waters from Hanlé-Gaggadé grabens (Republic of Djibouti, East African Rift System): a low-enthalpy geothermal resource from a transboundary aquifer. Geothermics 86, 101805. https://doi.org/10.1016/j.geothermics.2020.101805.

Azhar, A.S.B., Latiff, A.H.A., Lim, L.H., Godeke, S.H., 2019. Groundwater investigation of coastal aquifer in Brunei Darussalam using seismic refraction. Environ. Earth Sci. 78 (6), 1–17. https://doi.org/10.1007/s12665-019-8203-6.

Bagheri, R., Nadri, A., Raeisi, E., Eggenkamp, H.G.M., Kazemi, G.A., Montaseri, A., 2014a. Hydrochemical and isotopic ($\delta^{18}O$, $\delta^{2}H$, $^{87}Sr/^{86}Sr$, $\delta^{37}Cl$ and $\delta^{81}Br$) evidence for the origin of saline formation water in a gas reservoir. Chem. Geol. 384, 62–75. https://doi.org/10.1016/j.chemgeo.2014.06.017.

Bagheri, R., Nadri, A., Raeisi, E., Kazemi, G.A., Eggenkamp, H.G.M., Montaseri, A., 2014b. Origin of brine in the Kangan gasfield: isotopic and hydrogeochemical approaches. Environ. Earth Sci. 72 (4), 1055–1072. https://doi.org/10.1007/s12665-013-3022-7.

Banda, K.E., Mwandira, W., Jakobsen, R., Ogola, J., Nyambe, I., Larsen, F., 2019. Mechanism of salinity change and hydrochemical evolution of groundwater in the Machile-Zambezi Basin, South-western Zambia. J. Afr. Earth Sci. 153, 72–82. https://doi.org/10.1016/j.jafrearsci.2019.02.022.

Barzegar, R., Moghaddam, A.A., Nazemi, A.H., Adamowski, J., 2018. Evidence for the occurrence of hydrogeochemical processes in the groundwater of Khoy plain, Northwestern Iran, using ionic ratios and geochemical modeling. Environ. Earth Sci. 77 (16), 597. https://doi.org/10.1007/s12665-018-7782-y.

Bawoke, G.T., Anteneh, Z.L., Kehali, A.T., Mohammedyasin, M.S., Wudie, G., 2019. Hydrogeochemical and isotopic signatures of groundwater in the Andasa watershed, upper blue nile basin, northwestern Ethiopia. J. Afr. Earth Sci. 160, 103617 https://doi.org/10.1016/j.jafrearsci.2019.103617.

Belkhiri, L., Mouni, L., Narany, T.S., Tiri, A., 2017. Evaluation of potential health risk of heavy metals in groundwater using the integration of indicator kriging and multivariate statistical methods. Groundw. Sustain. Dev. 4, 12–22. https://doi.org/10.1016/j.gsd.2016.10.003.

Birks, S.J., Fennell, J.W., Gibson, J.J., Yi, Y., Moncur, M.C., Brewster, M., 2019. Using regional datasets of isotope geochemistry to resolve complex groundwater flow and formation connectivity in Northeastern Alberta, Canada. Appl. Geochem. 101, 140–159. https://doi.org/10.1016/j.apgeochem.2018.12.013.

Boschetti, T., Toscani, L., Shouakar-Stash, O., Iacumin, P., Venturelli, G., Mucchino, C., Frape, S.K., 2011. Salt waters of the northern Apennine Foredeep basin (Italy): origin and evolution. Aquat. Geochem. 17 (1), 71–108. https://doi.org/10.1007/s10498-010-9107-y.

Boschetti, T., Angulo, B., Cabrera, F., Vásquez, J., Montero, R.L., 2016. Hydrogeochemical characterization of oilfield waters from Southeast Maracaibo Basin (Venezuela): diagenetic effects on chemical and isotopic composition. Mar. Petrol. Geol. 73, 228–248. https://doi.org/10.1016/j.marpetgeo.2016.02.020.

Bozau, E., Sattler, C.D., Van Berk, W., 2015. Hydrogeochemical classification of deep formation waters. Appl. Geochem. 52, 23–30. https://doi.org/10.1016/j.apgeochem.2014.10.018.

Busico, G., Cuoco, E., Kazakis, N., Colombani, N., Mastrocicco, M., Tedesco, D., Voudouris, K., 2018. Multivariate statistical analysis to characterize/discriminate between anthropogenic and geogenic trace elements occurrence in the Campania Plain, Southern Italy. Environ. Pollut. 234, 260–269. https://doi.org/10.1016/j.envpol.2017.11.053.

Chabaane, A., Redhaounia, B., Gabtni, H., 2017. Combined application of vertical electrical sounding and 2D electrical resistivity imaging for geothermal groundwater characterization: Hammam Sayala hot spring case study (NW Tunisia). J. Afr. Earth Sci. 134, 292–298. https://doi.org/10.1016/j.jafrearsci.2017.07.003.

Chander, V., Tewari, D., Negi, V., Singh, R., Upadhyaya, K., Aleya, L., 2020. Structural characterization of Himalayan black rock salt by SEM, XRD and in-vitro antioxidant activity. Sci. Total Environ., 141269 https://doi.org/10.1016/j.scitotenv.2020.141269.

Chidambaram, S., Prasanna, M.V., Venkatramanan, S., Nepolian, M., Pradeep, K., Banajarani, P., Thivya, C., Thilagavathi, R., 2022a. Groundwater quality assessment for irrigation by adopting new suitability plot and spatial analysis based on fuzzy logic technique. Environ. Res. 204 (2022), 111729 https://doi.org/10.1016/j.envres.2021.111729.

Chidambaram, S., Banajarani, P., Tirumelash, K., Prasanna, M.V., Dhiraj, S., Ramanathan, A.L., 2022b. Isotopic signatures to address the groundwater recharge in coastal aquifers. Mar. Pollut. Bull. 174 (2022), 113273 https://doi.org/10.1016/j.marpolbul.2021.113273.

Clark, I., 2015. Groundwater Geochemistry and Isotopes. CRC press, pp. 24–28.

Coplen, T.B., 1994. Reporting of stable hydrogen, carbon, and oxygen isotopic abundances (technical report). Pure Appl. Chem. 66 (2), 273–276. https://doi.org/10.1351/pac199466020273.

Craig, H., 1961. Isotopic variations in meteoric waters. Science 133 (3465), 1702–1703.

Cullen B, A, 2010. Transverse segmentation of the Baram-Balabac Basin, NW Borneo: refining the model of Borneo's tectonic evolution. Petrol. Geosci. 16 (1), 3–29. https://doi.org/10.1144/1354-079309-828.

Dansgaard, W., 1964. Stable isotopes in precipitation. Tellus 16 (4), 436–468. https://doi.org/10.3402/tellusa.v16i4.8993.

Desper, D.B., Link, C.A., Nelson, P.N., 2015. Accurate water-table depth estimation using seismic refraction in areas of rapidly varying subsurface conditions. Near Surf. Geophys. 13 (5), 455–467. https://doi.org/10.3997/1873-0604.2015039.

Devaraj, N., Chidambaram, S., Gantayat, R.R., Thivya, C., Thilagavathi, R., Prasanna, M.V., Paramaguru, P., 2018. An insight on the speciation and genetical imprint of bicarbonate ion in the groundwater along K/T boundary, South India. Arabian J. Geosci. 11 (12), 291. https://doi.org/10.1007/s12517-018-3622-3.

Dezayes, C., Lerouge, C., Sanjuan, B., Ramboz, C., Brach, M., 2015. Toward a Better Understanding of the Fluid Circulation in the Rhine Graben for a Better Geothermal Exploration of the Deep Basins.

Dişli, E., Gülyüz, N., 2020. Hydrogeochemical investigation of an epithermal mineralization bearing basin using multivariate statistical techniques and isotopic

evidence of groundwater: Kestanelik Sub-Basin, Lapseki, Turkey. Geochemistry, 125661. https://doi.org/10.1016/j.chemer.2020.125661.
Du, Y., Ma, T., Chen, L., Xiao, C., Liu, C., 2016. Chlorine isotopic constraint on contrastive genesis of representative coastal and inland shallow brine in China. J. Geochem. Explor. 170, 21–29. https://doi.org/10.1016/j.gexplo.2016.07.024.
Drever I, J, 1988. The geochemistry of natural waters, Vol. 437. Prentice hall, Englewood Cliffs.
Du, Y., Fan, Q., Gao, D., Wei, H., Shan, F., Li, B., Teng, X., 2019. Evaluation of boron isotopes in halite as an indicator of the salinity of Qarhan paleolake water in the Eastern Qaidam Basin, western China. Geosci. Front. 10 (1), 253–262. https://doi.org/10.1016/j.gsf.2018.02.016.
Duan, R., Li, P., Wang, L., He, X., Zhang, L., 2022. Hydrochemical characteristics, hydrochemical processes and recharge sources of the geothermal systems in Lanzhou City, northwestern China. Urban Clim. 43, 101152 https://doi.org/10.1016/j.uclim.2022.101152.
Durov, S.A., 1948. Natural waters and graphic representation of their composition. Dokl. Akad. Nauk SSSR 59 (3), 87–90.
Ehya, F., Marbouti, Z., 2016. Hydrochemistry and contamination of groundwater resources in the Behbahan plain, SW Iran. Environ. Earth Sci. 75 (6), 455. https://doi.org/10.1007/s12665-016-5320-3.
Engle, M.A., Reyes, F.R., Varonka, M.S., Orem, W.H., Ma, L., Ianno, A.J., Carroll, K.C., 2016. Geochemistry of formation waters from the Wolfcamp and "Cline" shales: insights into brine origin, reservoir connectivity, and fluid flow in the Permian Basin, USA. Chem. Geol. 425, 76–92. https://doi.org/10.1016/j.chemgeo.2016.01.025.
Ercan, H.Ü., Karakaya, M.Ç., Bozdağ, A., Karakaya, N., Delikan, A., 2019. Origin and evolution of halite based on stable isotopes (δ^{37}Cl, δ^{81}Br, δ^{11}B and δ^{7}Li) and trace elements in Tuz Gölü Basin, Turkey. Appl. Geochem. 105, 17–30. https://doi.org/10.1016/j.apgeochem.2019.04.008.
Esmaeili, S., Moghaddam, A.A., Barzegar, R., Tziritis, E., 2018. Multivariate statistics and hydrogeochemical modeling for source identification of major elements and heavy metals in the groundwater of Qareh-Ziaeddin plain, NW Iran. Arabian J. Geosci. 11 (1), 5. https://doi.org/10.1007/s12517-017-3317-1.
Evans, N.P., Turchyn, A.V., Gázquez, F., Bontognali, T.R., Chapman, H.J., Hodell, D.A., 2015. Coupled measurements of δ^{18}O and δD of hydration water and salinity of fluid inclusions in gypsum from the Messinian Yesares Member, Sorbas Basin (SE Spain). Earth Planet Sci. Lett. 430, 499–510. https://doi.org/10.1016/j.epsl.2015.07.071.
Fakharian, K., Narany, T.S., 2016. Multidisciplinary approach to evaluate groundwater salinity in Saveh Plain, Iran. Environ. Earth Sci. 75 (7), 624. https://doi.org/10.1007/s12665-015-5104-1.
Farid, I., Zouari, K., Rigane, A., Beji, R., 2015. Origin of the groundwater salinity and geochemical processes in detrital and carbonate aquifers: case of Chougafiya basin (Central Tunisia). J. Hydrol. 530, 508–532. https://doi.org/10.1016/j.jhydrol.2015.10.009.
Farid, A., Khalid, P., Jadoon, K.Z., Iqbal, M.A., Shafique, M., 2017. Applications of variogram modeling to electrical resistivity data for the occurrence and distribution of saline groundwater in Domail Plain, Northwestern Himalayan fold and thrust belt, Pakistan. J. Mt. Sci. 14 (1), 158–174. https://doi.org/10.1007/s11629-015-3754-9.
Fontes, J.C., Mantray, J.M., 1993. Geochemistry and origin of formation brines from the Paris Basin, France: 2. Saline solution associated with oil fields. Chem. Geol. 109 (1–4), 177–200. https://doi.org/10.1016/0009-2541(93)90069-U.
Freeze, R.A., Cherry, J.A., 1979. In: Groundwater: New Jersey. Englewood Cliffs.
Galin, T., Breitfeld, H.T., Hall, R., Sevastjanova, I., 2017. Provenance of the Cretaceous-Eocene Rajang Group submarine fan, Sarawak, Malaysia from light and heavy mineral assemblages and U-Pb zircon geochronology. Gondwana Res. 51, 209–233. https://doi.org/10.1016/j.gr.2017.07.016.
Gautam, M.K., Lee, K.S., Bong, Y.S., Song, B.Y., Ryu, J.S., 2017. Oxygen and hydrogen isotopic characterization of rainfall and throughfall in four South Korean cool temperate forests. Hydrol. Sci. J. 62 (12), 2025–2034. https://doi.org/10.1080/02626667.2017.1358813.
Gibbs, R.J., 1970. Mechanisms controlling world water chemistry. Science 170 (3962), 1088–1090. https://doi.org/10.1126/science.170.3962.1088.
Gil-Márquez, J.M., Barberá, J.A., Andreo, B., Mudarra, M., 2017. Hydrological and geochemical processes constraining groundwater salinity in wetland areas related to evaporitic (karst) systems. A case study from Southern Spain. J. Hydrol. 544, 538–554. https://doi.org/10.1016/j.jhydrol.2016.11.062.
Glas, R., Lautz, L., McKenzie, J., Moucha, R., Chavez, D., Mark, B., Lane, J.W., 2019. Hydrogeology of an alpine talus aquifer: Cordillera Blanca, Peru. Hydrogeol. J. 1–18. https://doi.org/10.1007/s10040-019-01982-5.
Gómez, E., Larsson, M., Dahlin, T., Barmen, G., Rosberg, J.E., 2019. Alluvial aquifer thickness and bedrock structure delineation by electromagnetic methods in the highlands of Bolivia. Environ. Earth Sci. 78 (3), 1–13. https://doi.org/10.1007/s12665-019-8074-x.
Ha, Q.K., Kim, K., Phan, N.L., Phung, T.H., Lee, J., Nguyen, V.K., Phan, C.N., 2019. A hydrogeological and geochemical review of groundwater issues in Southern Vietnam. Geosci. J. 23 (6), 1005–1023. https://doi.org/10.1007/s12303-019-0021-z.
Haile, N.S., 1962. The Geology and Mineral Resources of the Suai-Baram Area. Geological Survey Department British Territories in Borneo.
Hall, R., 2013. Contraction and extension in Northern Borneo driven by subduction rollback. J. Asian Earth Sci. 76, 399–411. https://doi.org/10.1016/j.jseaes.2013.04.010.
Han, J.L., Han, F.Q., Hussain, S.A., Liu, W.Y., Nian, X.Q., Mao, Q.F., 2018. Origin of boron and brine evolution in saline springs in the Nangqen Basin, Southern Tibetan Plateau. Geofluids. https://doi.org/10.1155/2018/1985784, 2018.
He, S., Li, P., Su, F., Wang, D., Ren, X., 2022. Identification and apportionment of shallow groundwater nitrate pollution in Weining Plain, northwest China, using hydrochemical indices nitrate stable isotopes, and the new Bayesian stable isotope mixing model (Mix SIAR). Environ. Pollut. 298, 118852 https://doi.org/10.1016/j.envpol.2022.118852.
Hem, J.D., 1985. Study and Interpretation of the Chemical Characteristic of Natural Water, vol. 2254. Department of the interior, US Geological Survey.
Hounslow W, A, 1995. Water Quality Data: Analysis and Interpretation (1st ed.). CRC press. https://doi.org/10.1201/9780203734117.
Hutchison, C.S., 2005. Geology of North-West Borneo: Sarawak, Brunei and Sabah. Elsevier.
Hutchison, C.S., 2010. Oroclines and paleomagnetism in Borneo and south-east Asia. Tectonophysics 496 (1–4), 53–67. https://doi.org/10.1016/j.tecto.2010.10.008.
Ibrahim, R.G.M., Korany, E.A., Tempel, R.N., Gomaa, M.A., 2019. Processes of water–rock interactions and their impacts upon the groundwater composition in Assiut area, Egypt: applications of hydrogeochemical and multivariate analysis. J. Afr. Earth Sci. 149, 72–83. https://doi.org/10.1016/j.jafrearsci.2018.07.026.
Isawi, H., El-Sayed, M.H., Eissa, M., Shouakar-Stash, O., Shawky, H., Mottaleb, M.S.A., 2016. Integrated geochemistry, isotopes, and geostatistical techniques to investigate groundwater sources and salinization origin in the Sharm EL-Shiekh Area, South Sinia, Egypt. Water, Air Soil Pollut. 227 (5), 151. https://doi.org/10.1007/s11270-016-2848-5.
Islami, N., Taib, S.H., Yusoff, I., Ghani, A.A., 2018. Integrated geoelectrical resistivity and hydrogeochemical methods for delineating and mapping heavy metal zone in aquifer system. Environ. Earth Sci. 77 (10), 383. https://doi.org/10.1007/s12665-018-7574-4.
Jagadeshan, G., Gosaye, B., Zinabe, S., Abeje, A., 2018. Assessment of groundwater potential using seismic refraction method in Secha, Arba Minch, Ethiopia. IOSR J. Appl. Geol. Geophys. 6 (1), 18–24. https://doi.org/10.9790/90990-0601011824.
Jankowski, J., Acworth, R.I., 1997. Impact of debris-flow deposits on hydrogeochemical processes and the development of dryland salinity in the Yass River Catchment, New South Wales, Australia. Hydrogeol. J. 5 (4), 71–88. https://doi.org/10.1007/s100400050119.
Jia, Y., Guo, H., Xi, B., Jiang, Y., Zhang, Z., Yuan, R., Xue, X., 2017. Sources of groundwater salinity and potential impact on arsenic mobility in the western Hetao Basin, Inner Mongolia. Sci. Total Environ. 601, 691–702. https://doi.org/10.1016/j.scitotenv.2017.05.196.
Jia, Y., Xi, B., Jiang, Y., Guo, H., Yang, Y., Lian, X., Han, S., 2018. Distribution, formation and human-induced evolution of geogenic contaminated groundwater in China: a review. Sci. Total Environ. 643, 967–993.
Kaown, D., Koh, D.C., Hakyeong, E.Y., Kim, H., Yoon, Y.Y., Yum, B.W., Lee, K.K., 2020. Combined effects of recharge and hydrogeochemical conditions on nitrate in groundwater of a highland agricultural basin based on multiple environmental tracers. Agric. Water Manag. 240, 106327 https://doi.org/10.1016/j.agwat.2020.106327.
Karakaya, M.Ç., Bozdağ, A., Ercan, H.Ü., Karakaya, N., Delikan, A., 2019. Origin of Miocene halite from Tuz Gölü basin in Central Anatolia, Turkey: evidences from the pure halite and fluid inclusion geochemistry. J. Geochem. Explor. 202, 1–12. https://doi.org/10.1016/j.gexplo.2019.03.004.
Kessler, F.L., Jong, J., Madon, M., 2019. The enigma of the Bario salt produced in the highlands of northern Sarawak. Warta Geol. 45 (2), 31–39. https://www.researchgate.net/publication/333775032.
Kloppmann, W., Négrel, P., Casanova, J., Klinge, H., Schelkes, K., Guerrot, C., 2001. Halite dissolution derived brines in the vicinity of a Permian salt dome (North German Basin). Evidence from boron, strontium, oxygen, and hydrogen isotopes. Geochem. Cosmochim. Acta 65 (22), 4087–4101. https://doi.org/10.1016/S0016-7037(01)00640-8.
Kura, N.U., Ramli, M.F., Sulaiman, W.N.A., Ibrahim, S., Aris, A.Z., 2018. An overview of groundwater chemistry studies in Malaysia. Environ. Sci. Pollut. Control Ser. 25 (8), 7231–7249. https://doi.org/10.1007/s11356-015-5957-6.
Langelier, W.F., Ludwig, H.F., 1942. Graphical methods for indicating the mineral character of natural waters. J. (Am. Water Works Assoc.) 34 (3), 335–352. https://doi.org/10.1002/j.1551-8833.1942.tb19682.x.
Li, P., Qian, H., Wu, J., 2018. Conjunctive use of groundwater and surface water to reduce soil salinization in Yinchuan Plain, North-West China. Int. J. Water Resour. Dev. 34 (3), 337–353. https://doi.org/10.1080/07900627.2018.1443059.
Li, C., Gao, X., Liu, Y., Wang, Y., 2019a. Impact of anthropogenic activities on the enrichment of fluoride and salinity in groundwater in the Yuncheng Basin constrained by Cl/Br ratio, δ^{18}O, δ^{2}H, δ^{13}C and δ^{7}Li isotopes. J. Hydrol. 579, 124211 https://doi.org/10.1016/j.jhydrol.2019.124211.
Li, P., Tian, R., Liu, R., 2019b. Solute geochemistry and multivariate analysis of water quality in the Guohua phosphorite mine, Guizhou Province, China. Expos. Health 11 (2), 81–94. https://doi.org/10.1007/s12403-018-0277-y.
Li, M., Fang, X., Li, J., Yan, M., Sun, S., Zhu, L., 2019c. Isotopic application in high saline conditions. In: Isotopes Applications in Earth Sciences. IntechOpen.
Lindholm, R., 2012. A Practical Approach to Sedimentology. Springer Science & Business Media.
Liu, C.W., Lu, K.L., Kao, Y.H., Wang, C.J., Maji, S.K., Lee, J.F., 2014. Identifying sources and controlling factors of arsenic release in saline groundwater aquifers. Hydrol. Earth Syst. Sci. 18 (3), 1089–1103. https://doi.org/10.5194/hess-18-1089-2014.
Liu, J., Chen, Z., Wang, L., Zhang, Y., Li, Z., Xu, J., Peng, Y., 2016. Chemical and isotopic constrains on the origin of brine and saline groundwater in Hetao plain, Inner Mongolia. Environ. Sci. Pollut. Control Ser. 23 (15), 15003–15014. https://doi.org/10.1007/s11356-016-6617-1.
Liu, J., Jin, D., Wang, T., Gao, M., Yang, J., Wang, Q., 2019. Hydrogeochemical processes and quality assessment of shallow groundwater in Chenqi coalfield, Inner Mongolia, China. Environ. Earth Sci. 78 (12), 347. https://doi.org/10.1007/s12665-019-8355-4.

Lloyd, J.W., Heathcote, J.A.A., 1985. Natural Inorganic Hydrochemistry in Relation to Groundwater. Clarendon Press, Oxford.
Lyu, M., Pang, Z., Yin, L., Zhang, J., Huang, T., Yang, S., Gulbostan, T., 2019. The control of groundwater flow systems and geochemical processes on groundwater chemistry: a case study in Wushenzhao basin, NW China. Water 11 (4), 790. https://doi.org/10.3390/w11040790.
Madzin, Z., Kusin, F.M., Yusof, F.M., Muhammad, S.N., 2017. Assessment of water quality index and heavy metal contamination in active and abandoned iron ore mining sites in Pahang, Malaysia. In: MATEC Web of Conferences, vol. 103. EDP Sciences, 05010. https://doi.org/10.1051/matecconf/201710305010.
Mahalakshmi, M., Chidambaram, S., Prasanna, M.V., Venkatramanan, S., Devaraj, N., Gunarani, G.I., Gnanasekar, M., Sahoo, S.K., 2022. Mobilization and health risk assessment of fertilizer induced uranium in coastal groundwater. Environ. Res. 203 (2022), 111791.
Mahmoud, H.H., Ghoubachi, S.Y., 2017. Geophysical and hydrogeological investigation to study groundwater occurrences in the Taref formation, south Mut area–Dakhla Oasis-Egypt. J. Afr. Earth Sci. 129, 610–622. https://doi.org/10.1016/j.jafrearsci.2017.02.009.
Mainoo, P.A., Manu, E., Yidana, S.M., Agyekum, W.A., Stigter, T., Duah, A.A., Preko, K., 2019. Application of 2D Electrical Resistivity Tomography in delineating groundwater potential zones: case study from the voltaian super group of Ghana. J. Afr. Earth Sci. 160, 103618 https://doi.org/10.1016/j.jafrearsci.2019.103618.
Marandi, A., Shand, P., 2018. Groundwater chemistry and the Gibbs diagram. Appl. Geochem. 97, 209–212. https://doi.org/10.1016/j.apgeochem.2018.07.009.
Martin, C., Flores, K.E., Harlow, G.E., 2016. Boron isotopic discrimination for subduction-related serpentinites. Geology 44 (11), 899–902. https://doi.org/10.1130/G38102.1.
Mateo-Sagasta, J., Zadeh, S.M., Turral, H., Burke, J., 2017. Water Pollution from Agriculture: a Global Review. Food and Agriculture Organization of the United Nations and the International Water Management Institute, Rome.
Mattos, J.B., Cruz, M.J.M., De Paula, F.C.F., Sales, E.F., 2018a. Natural and anthropic processes controlling groundwater hydrogeochemistry in a tourist destination in northeastern Brazil. Environ. Monit. Assess. 190 (7), 395. https://doi.org/10.1007/s10661-018-6765-5.
Mattos, J.B., Cruz, M.J.M., De Paula, F.C.F., Sales, E.F., 2018b. Spatio-seasonal changes in the hydrogeochemistry of groundwaters in a highland tropical zone. J. S. Am. Earth Sci. 88, 275–286. https://doi.org/10.1016/j.jsames.2018.08.023.
McHenry, L.J., Kodikara, G.L., Stanistreet, I.G., Stollhofen, H., Njau, J.K., Schick, K., Toth, N., 2020. Lake conditions and detrital sources of Paleolake Olduvai, Tanzania, reconstructed using X-ray Diffraction analysis of cores. Palaeogeogr. Palaeoclimatol. Palaeoecol. https://doi.org/10.1016/j.palaeo.2020.109855, 109855.
Mejri, S., Chekirbene, A., Tsujimura, M., Boughdiri, M., Mlayah, A., 2018. Tracing groundwater salinization processes in an inland aquifer: a hydrogeochemical and isotopic approach in Sminja aquifer (Zaghouan, Northeast of Tunisia). J. Afr. Earth Sci. 147, 511–522. https://doi.org/10.1016/j.jafrearsci.2018.07.009.
Mgbenu, C.N., Egbueri, J.C., 2019. The hydrogeochemical signatures, quality indices and health risk assessment of water resources in Umunya district, Southeast Nigeria. Appl. Water Sci. 9 (1), 22. https://doi.org/10.1007/s13201-019-0900-5.
Mirzavand, M., Ghasemieh, H., Sadatinejad, S.J., Bagheri, R., 2020a. An overview on source, mechanism and investigation approaches in groundwater salinization studies. Int. J. Environ. Sci. Technol. 1–14. https://doi.org/10.1007/s13762-020-02647-7.
Mirzavand, M., Ghasemieh, H., Sadatinejad, S.J., Bagheri, R., 2020b. Delineating the source and mechanism of groundwater salinization in crucial declining aquifer using multi-chemo-isotopes approaches. J. Hydrol., 124877 https://doi.org/10.1016/j.jhydrol.2020.124877.
Mohamaden, M.I.I., Hamouda, A.Z., Mansour, S., 2016. Application of electrical resistivity method for groundwater exploration at the Moghra area, Western Desert, Egypt. Egypt. J. Aquat. Res. 42 (3), 261–268. https://doi.org/10.1016/j.ejar.2016.06.002.
Morley, C.K., Tingay, M., Hillis, R., King, R., 2008. Relationship between structural style, overpressures, and modern stress, Baram delta Province, northwest Borneo. J. Geophys. Res. Solid Earth 113 (B9). https://doi.org/10.1029/2007JB005324.
Mosaad, S., Kehew, A.E., 2019. Integration of geochemical data to assess the groundwater quality in a carbonate aquifer in the southeast of Beni-Suef city, Egypt. J. Afr. Earth Sci. 158, 103558 https://doi.org/10.1016/j.jafrearsci.2019.103558.
Musashi, M., Oi, T., Kreulen, R., 2015. Chlorine isotopic compositions of deep saline fluids in Ibusuki coastal geothermal region, Japan: using B–Cl isotopes to interpret fluid sources. Isot. Environ. Health Stud. 51 (2), 285–299. https://doi.org/10.1080/10256016.2015.997722.
Nagarajan, R., Kessler, F.L., Jong, J., Ramkumar, Mu., Abdulmajid Muhammad, A., Vivivan, D., Desianne, K.S., et al., 2021. Geochemistry of the Palaeocene-eocene upper Kelalan Formation, NW Borneo: implications on palaeoweathering, tectonic setting, and provenance. Geol. J. 56, 2500–2527. https://doi.org/10.1002/gj.3950.
Nazaruddin, D.A., Amiruzan, Z.S., Hussin, H., Jafar, M.T.M., 2017. Integrated geological and multi-electrode resistivity surveys for groundwater investigation in Kampung Rahmat village and its vicinity, Jeli district, Kelantan, Malaysia. J. Appl. Geophys. 138, 23–32. https://doi.org/10.1016/j.jappgeo.2017.01.012.
Nepolian, M., Chidambaram, S., Prasanna, M.V., Venkatramanan, S., Selvam, S., Devaraj, N., Gnanachandrasamy, G., Mahalakshmi, M., 2022. Source, mobilization and distribution of uranium in a complex aquifer system: a spatial and temporal evaluation using geochemical, statistics and GIS approach. Environ. Earth Sci. 81, 192.
Ninu Krishnan, M.V., Prasanna, M.V., Vijith, H., 2019. Statistical analysis of trends in monthly precipitation at the Limbang river basin, Sarawak (NW Borneo), Malaysia. Meteorol. Atmos. Phys. 131 (4), 883–896. https://doi.org/10.1007/s00703-018-0611-8.
Ninu Krishnan, M.V., Prasanna, M.V., Vijith, H., Chidambaram, S., 2022. Isoscapes to address the regional precipitation trends in the equatorial region of Southeast Asia. Phys. Chem. Earth, Parts A/B/C, 103159. https://doi.org/10.1016/j.pce.2022.103159.
Oskooi, B., Moradi, M., Smirnov, M., 2019. Integrated interpretation of seismic and magnetotelluric data on Shurab diapirs in Qom basin, Central Iran. Acta Geophys. 1–20. https://doi.org/10.1007/s11600-019-00286-2.
Oyem, H.H., Oyem, I.M., Obiwulu, E.N., 2017. Barium, calcium and sodium, cyanide, phosphate and sulphate contents of groundwater in some ika communities of delta state, Nigeria. J. Geosci. Environ. Protect. 5 (8), 89–98. https://doi.org/10.4236/gep.2017.58009.
Özdemir, A., 2018. Iodine-rich waters of Turkey and oil & gas potential of the onshore. J. Sustain. Eng. 1 (2).
Parkhurst, D.L., Appelo, C.A.J., 1999. User's guide to PHREEQC (Version 2): a computer program for speciation, batch-reaction, one-dimensional transport, and inverse geochemical calculations. Water-Resour. Invest. Rep. 99 (4259), 312.
Pholkern, K., Saraphirom, P., Srisuk, K., 2018. Potential impact of climate change on groundwater resources in the Central Huai Luang basin, northeast Thailand. Sci. Total Environ. 633, 1518–1535. https://doi.org/10.1016/j.scitotenv.2018.03.300.
Piper, A.M., 1944. A graphic procedure in the geochemical interpretation of water-analyses. Eos, Trans. Am. Geophys. Union 25 (6), 914–928. https://doi.org/10.1029/TR025i006p00914.
Pisciotta, A., Tiwari, A.K., De Maio, M., 2019. An integrated multivariate statistical analysis and hydrogeochemical approaches to identify the major factors governing the chemistry of water resources in a mountain region of Northwest Italy. Carbonates Evaporites 34 (3), 955–973. https://doi.org/10.1007/s13146-018-0452-z.
Prasanna, M.V., Nagarajan, R., Chidambaram, S., Anand Kumar, A., Thivya, C., 2017. Evaluation of hydrogeochemical characteristics and the impact of weathering in seepage water collected within the sedimentary formation. Acta Geochemica 36 (1), 44–51.
Purnomo, B.J., Pichler, T., You, C.F., 2016. Boron isotope variations in geothermal systems on Java, Indonesia. J. Volcanol. Geoth. Res. 311, 1–8. https://doi.org/10.1016/j.jvolgeores.2015.12.014.
Quattrini, S., Pampaloni, B., Brandi, M.L., 2016. Natural mineral waters: chemical characteristics and health effects. Clin. Cases Miner. Bone Metab. 13 (3), 173. https://doi.org/10.11138/ccmbm/2016.13.3.173.
Ramesh, R., Anbu, M., 1996. Chemical Methods for Environmental Analysis: Water and Sediment. Macmillan India.
Rehman, F., Abuelnaga, H.S., Harbi, H.M., Cheema, T., Atef, A.H., 2016. Using a combined electrical resistivity imaging and induced polarization techniques with the chemical analysis in determining of groundwater pollution at Al Misk Lake, Eastern Jeddah, Saudi Arabia. Arabian J. Geosci. 9 (4), 286. https://doi.org/10.1007/s12517-016-2423-9.
Rusydi, A.F., 2018. Correlation between conductivity and total dissolved solid in various type of water: a review. In: IOP Conference Series: Earth and Environmental Science, vol. 118, 012019. No. 1 IOP Publishing.
Samantara, M.K., Padhi, R.K., Sowmya, M., Kumaran, P., Satpathy, K.K., 2017. Heavy Metal Contamination, Major Ion Chemistry and Appraisal of the Groundwater Status in Coastal Aquifer, Kalpakkam, Tamil Nadu, India, vol. 5. Groundwater for Sustainable Development, pp. 49–58. https://doi.org/10.1016/j.gsd.2017.04.001.
Sarikhani, R., Dehnavi, A.G., Ahmadnejad, Z., Kalantari, N., 2015. Hydrochemical characteristics and groundwater quality assessment in Bushehr Province, SW Iran. Environ. Earth Sci. 74 (7), 6265–6281. https://doi.org/10.1007/s12665-015-4651-9.
Saw, B.B., Schlaich, M., Pöppelreiter, M.C., Ramkumar, M., Lunt, P., Vintaned, J.A.G., Ali, S.H., 2019. Facies, depositional environments, and anatomy of the Subis build-up in Sarawak, Malaysia: implications on other Miocene isolated carbonate build-ups. Facies 65 (3), 28. https://doi.org/10.1007/s10347-019-0571-6.
Sefie, A., Aris, A.Z., Ramli, M.F., Narany, T.S., Shamsuddin, M.K.N., Saadudin, S.B., Zali, M.A., 2018. Hydrogeochemistry and groundwater quality assessment of the multilayered aquifer in Lower Kelantan Basin, Kelantan, Malaysia. Environ. Earth Sci. 77 (10), 397. https://doi.org/10.1007/s12665-018-7561-9.
Selvam, S., Jesuraja, K., Venkatramanan, S., Chidambaram, S., Prasanna, M.V., Sivakumar, K., 2021. Delineation saline and fresh water aquifers in Tuticorin of southern India by using geophysical techniques. Environ. Dev. Sustain. https://doi.org/10.1007/s10668-021-01409-w.
Sheikhy Narany, T., Ramli, M.F., Aris, A.Z., Sulaiman, W.N.A., Juahir, H., Fakharian, K., 2014. Identification of the hydrogeochemical processes in groundwater using classic integrated geochemical methods and geostatistical techniques. In: Amol-Babol Plain. The Scientific World Journal, Iran, pp. 1–15. https://doi.org/10.1155/2014/419058, 2014.
Sherif, M.I., Sultan, M., Sturchio, N.C., 2019. Chlorine isotopes as tracers of solute origin and age of groundwaters from the Eastern Desert of Egypt. Earth Planet Sci. Lett. 510, 37–44. https://doi.org/10.1016/j.epsl.2018.12.035.
Shouakar-Stash, O., Alexeev, S.V., Frape, S.K., Alexeeva, L.P., Drimmie, R.J., 2007. Geochemistry and stable isotopic signature, including chlorine and bromine isotopes, of the deep groundwaters of the Siberian Platform, Russia. Appl. Geochem. 22 (3), 589–605. https://doi.org/10.1016/j.apgeochem.2006.12.005.
Singh, C.K., Kumar, A., Shashtri, S., Kumar, A., Kumar, P., Mallick, J., 2017. Multivariate statistical analysis and geochemical modeling for geochemical assessment of groundwater of Delhi, India. J. Geochem. Explor. 175, 59–71. https://doi.org/10.1016/j.gexplo.2017.01.001.
Sivakarun, N., Udayaganeshan, P., Chidambaram, S., Venkatramanan, S., Prasanna, M.V., Pradeep, K., Banajarani, P., 2020. Factors determining the hydrogeochemical

processes occurring in shallow groundwater of coastal alluvial aquifer, India. Geochemistry 80, 125623.
Sun, Z., Ma, R., Wang, Y., Hu, Y., Sun, L., 2016. Hydrogeological and hydrogeochemical control of groundwater salinity in an arid inland basin: Dunhuang Basin, Northwestern China. Hydrol. Process. 30 (12), 1884–1902. https://doi.org/10.1002/hyp.10760.
Szynkiewicz, A., Olichwer, T., Tarka, R., 2020. Delineation of groundwater provenance in Arctic environment using isotopic compositions of water and sulphate. J. Hydrol. 580, 124232 https://doi.org/10.1016/j.jhydrol.2019.124232.
Thapa, B.R., Shrestha, S.R., Okwany, R.O., Neupane, M., 2019. Shallow aquifer potential mapping in the foothills of Churia in eastern Gangetic plain of Saptari district, Nepal. Appl. Water Sci. 9 (4), 92. https://doi.org/10.1007/s13201-019-0971-3.
Thivya, C., Chidambaram, S., Thilagavathi, R., Prasanna, M.V., Singaraja, C., Adithya, V. S., Nepolian, M., 2015. A multivariate statistical approach to identify the spatio-temporal variation of geochemical process in a hard rock aquifer. Environ. Monit. Assess. 187, 552. http://link.springer.com/article/10.1007/s10661-015-4738-5.
Thivya, C., Chidambaram, S., Rao, M.S., Gopalakrishnan, M., Thilagavathi, R., Prasanna, M.V., Nepolian, M., 2016. Identification of recharge processes in groundwater in hard rock aquifers of Madurai District using stable isotopes. Environ. Proc. 3 (2), 463–477. https://doi.org/10.1007/s40710-016-0137-3.
Thivya, C., Tirumalesh, K., Gnanachandrasamy, G., Shankar, K., Venkatramanan, S., Chidambaram, S., Prasanna, M.V., 2021. Occurrence of heavy metals in groundwater along the lithological interface of K/T boundary, Peninsular India: a special focus on source, geochemical mobility and health risk. Arch. Environ. Contam. Toxicol. 80, 183–207.
Torres-Martínez, J.A., Mora, A., Knappett, P.S., Ornelas-Soto, N., Mahlknecht, J., 2020. Tracking nitrate and sulfate sources in groundwater of an urbanized valley using a multi-tracer approach combined with a Bayesian isotope mixing model. Water Res. https://doi.org/10.1016/j.watres.2020.115962, 115962.
Tostevin, R., Craw, D., Van Hale, R., Vaughan, M., 2016. Sources of environmental sulfur in the groundwater system, Southern New Zealand. Appl. Geochem. 70, 1–16. https://doi.org/10.1016/j.apgeochem.2016.05.005.
Urrutia, J., Guimerà, J., Custodio, E., Herrera, C., Jódar, J., Acosta, O., Ansón, I., 2021. Processes Explaining the Origin and Evolution of Groundwater Composition in the Andean Precordillera and Altiplano of the Tarapacá Region of Northern Chile. Science of The Total Environment. https://doi.org/10.1016/j.scitotenv.2021.149742, 149742.
Van Engelen, J., Essink, G.H.O., Kooi, H., Bierkens, M.F., 2018. On the origins of hypersaline groundwater in the Nile Delta aquifer. J. Hydrol. 560, 301–317. https://doi.org/10.1016/j.jhydrol.2018.03.029.
Van Hattum, M.W.A., Hall, R., Pickard, A.L., Nichols, G.J., 2013. Provenance and geochronology of cenozoic sandstones of northern Borneo. J. Asian Earth Sci. 76, 266–282. https://doi.org/10.1016/j.jseaes.2013.02.033.
Van Weert, F., Van der Gun, J., Reckman, J., 2009. Global overview of saline groundwater occurrence and genesis. Int. Groundw. Resour. Assess. Centre. http://www.igrac.net.
Vengosh, A., 2014. Environmental geochemistry, 11.9 salinization and saline environments. Treatise Geochem. ume 11, 325–378. https://dx.doi:10.1016.B978-0-08-095975-7.00909-8.
Vishwakarma, C.A., Sen, R., Singh, N., Singh, P., Rena, V., Rina, K., Mukherjee, S., 2018. Geochemical characterization and controlling factors of chemical composition of spring water in a part of Eastern Himalaya. J. Geol. Soc. India 92 (6), 753–763. https://doi.org/10.1007/s12594-018-1098-0.
Walter, J., Chesnaux, R., Cloutier, V., Gaboury, D., 2017. The influence of water/rock–water/clay interactions and mixing in the salinization processes of groundwater. J. Hydrol.: Reg. Stud. 13, 168–188. https://doi.org/10.1016/j.ejrh.2017.07.004.
Wang, H., Zhang, Q., 2019. Research advances in identifying sulfate contamination sources of water environment by using stable isotopes. Int. J. Environ. Res. Publ. Health 16 (11), 1914. https://doi.org/10.3390/ijerph16111914.
Wang, P.C., Li, S.Z., Guo, L.L., Jiang, S.H., Somerville, I.D., Zhao, S.J., Han, B., 2016. Mesozoic and Cenozoic accretionary orogenic processes in Borneo and their mechanisms. Geol. J. 51, 464–489. https://doi.org/10.1002/gj.2835.
Wannier, M., 2009. Carbonate platforms in wedge-top basins: an example from the Gunung Mulu National Park, northern Sarawak (Malaysia). Mar. Petrol. Geol. 26 (2), 177–207. https://doi.org/10.1016/j.marpetgeo.2007.12.004.
Wirmvem, M.J., Kamtchueng, B.T., Wotany, E.R., Mimba, M.E., Fantong, W.Y., Ako, A. A., Ohba, T., 2020. Multi-tracer (δ18O, δD, 3H, CFCs and SF6) investigation of groundwater recharge and apparent age at the Bamenda Highlands along the Cameroon volcanic line. Sustain. Water Resour. Manag. 6 (1), 1–16. https://doi.org/10.1007/s40899-020-00357-z.
World Wildlife Fund Malaysia, 2005. The Conservation and Sustainable Use of the Highlands of Sabah & Sarawak Preliminary Report. Issue 1.0. Retrieved from. https://repository.wwf.org.my/technical_reports/P/PolicyStrategiesForTheConservationAndSustainableUseOfTheHighlandsOfSabahAndSarawakPreliminaryReport.pdf.
Wu, J., Wang, D., Ren, X., Wei, M., 2020. Statistical and multivariate statistical techniques to trace the sources and affecting factors of groundwater pollution in a rapidly growing city on the Chinese Loess Plateau. Hum. Ecol. Risk Assess. 26 (6), 1603–1621. https://doi.org/10.1080/10807039.2019.1594156.
Xiang, W., Si, B.C., Biswas, A., Li, Z., 2019. Quantifying dual recharge mechanisms in deep unsaturated zone of Chinese Loess Plateau using stable isotopes. Geoderma 337, 773–781. https://doi.org/10.1016/j.geoderma.2018.10.006.
Zaidi, F.K., Nazzal, Y., Jafri, M.K., Naeem, M., Ahmed, I., 2015. Reverse ion exchange as a major process controlling the groundwater chemistry in an arid environment: a case study from Northwestern Saudi Arabia. Environ. Monit. Assess. 187 (10), 607. https://doi.org/10.1007/s10661-015-4828-4.
Zhang, Q., Wang, H., Lu, C., 2020. Tracing sulfate origin and transformation in an area with multiple sources of pollution in northern China by using environmental isotopes and Bayesian isotope mixing model. Environ. Pollut. 265, 115105 https://doi.org/10.1016/j.envpol.2020.115105.
Zhang, L., Li, P., He, X., 2022. Interactions between surface water and groundwater in selected tributaries of the Wei River (China) revealed by hydrochemistry and stable isotopes. Hum. Ecol. Risk Assess. 28 (1), 79–99. https://doi.org/10.1080/10807039.2021.2016054.